



The role of size in the multiple scattering correction C for dual-spot aethalometer: a field and laboratory investigation

Laura Renzi¹, Claudia Di Biagio², Johannes Heuser³, Marco Zanatta^{1,2}, Mathieu Cazaunau³, Antonin Bergé², Edouard Pangui³, Jérôme Yon⁴, Tommaso Isolabella^{5,6}, Dario Massabò^{5,6}, Virginia Vernocchi⁶, Martina Mazzini¹, Chenjie Yu², Paola Formenti², Benedicte Picquet-Varrault³, Jean-Francois Doussin³, Angela Marinoni¹

¹ Institute of Atmospheric Sciences and Climate, National Research Council of Italy, Bologna, Italy

² Université Paris Cité and Univ Paris Est Creteil, CNRS, LISA, F-75013 Paris, France

³ Univ Paris Est Creteil and Université Paris Cité, CNRS, LISA, F-94010 Créteil, France

⁴ INSA Rouen Normandie, Univ. Rouen Normandie, CNRS, Normandie Univ., CORIA UMR 6614, 76000, Rouen France

⁵ Department of Physics, University of Genoa, Via Dodecaneso 33, 16146 Genoa, Italy

⁶ INFN – Division of Genoa, Via Dodecaneso 33, 16146 Genova, Italy

Correspondence to: Laura Renzi (l.renzi@isac.cnr.it)

Abstract. The dual-spot aethalometer AE33 is a widely used instrument for measuring the aerosol absorption coefficient, but the accuracy of its measurements is heavily dependent on the multiple scattering correction factor (C), which compensates for multiple scattering effects in the filter matrix. Despite its widespread use, the factors influencing variability of C remain poorly understood, particularly in relation to aerosol properties.

In this work, we explore the variability of C for the AE33 in a wide range of conditions and aerosol properties by combining chamber experiments with freshly emitted laboratory-generated soot and ambient data from a mountaintop site in Italy (Monte Cimone, CMN). The C factor is derived by comparison with independent filter-based instruments such as the MAAP (Multi-Angle Absorption Photometer) and MWAA (Multi-Wavelength Absorption Analyzer) at CMN and the extinction-minus-scattering (EMS) approach in chamber experiments.

The mean C value at a wavelength of 637 nm derived at CMN is 2.35 with a standard deviation of 0.58, while the average values obtained in chamber experiments in different conditions range from 2.89 ± 0.03 to 3.9 ± 0.06 . The variability of C at CMN appears to be primarily influenced by the signal-to-noise ratio of the instruments, especially during the colder months when absorption coefficient values fall below 1 Mm^{-1} . In contrast, in the chamber experiments, the variability is mainly driven by particle properties. The C value at 637 nm, derived from measurements at CMN, increases with increasing single scattering albedo (SSA), particularly for SSA values above 0.94, while showing no statistically significant spectral variability. Both ambient and chamber experiments highlight the dependence of the C factor on particle size, with C increasing as particle diameter decreases below 120 nm. This size dependence is relatively small (within 15%) under ambient conditions dominated by mostly scattering aerosols, but it leads to changes greater than 60% for highly absorbing soot particles.

1 Introduction

Absorbing aerosols have a unique and important role in the Earth's climate system (Bond et al., 2013; Liu et al., 2020a). By absorbing solar and terrestrial infrared radiation, aerosols exert an influence on low tropospheric temperature, liquid



42 and ice cloud distribution and properties, atmospheric dynamics, as well as surface reflectivity, in particular over snow
43 and ice surfaces (Ramanathan and Carmichael, 2008; Liu et al., 2020a; Li et al., 2022; Kok et al., 2023). This impact is
44 especially significant for strongly absorbing species such as black carbon (BC), brown carbon (BrC), and mineral dust.
45 These components account for the majority of aerosol light absorption and contribute substantially to the direct radiative
46 effect at both regional and global scales (e.g. Chung et al., 2012; Kok et al., 2023; Sand et al., 2021; Zhu et al., 2021).

47 The strength of this radiative effect is typically characterized by the aerosol absorption coefficient, expressed in inverse
48 mega meters (b_{abs} , Mm^{-1}) that represents the amount of light absorbed by aerosol per unit volume. The b_{abs} is commonly
49 measured using filter-based techniques, differential extinction-minus-scattering (EMS) methods, or photoacoustic
50 instruments. Despite its importance, aerosol absorption remains poorly constrained. This is primarily due to the lack of
51 standardized measurement approaches and the presence of instrument-specific biases (Petzold et al., 2013), which
52 introduce substantial uncertainties in b_{abs} data. In consequence, a major difficulty lies in capturing the magnitude and
53 spatio-temporal variability of the spectral mass absorption cross section (MAC, m^2g^{-1}), i.e. the absorption coefficient per
54 unit of absorbing specie mass concentration ($\mu\text{g m}^{-3}$), or the single scattering albedo (SSA), representing the fraction of
55 scattered radiation with respect to extinction. The MAC and SSA depend on a wide variety of variables such as the
56 composition (via the complex refractive index, CRI), size, morphology and mixing state of the particles (Liu et al., 2020b;
57 Moteki, 2023). Understanding these dependencies is required for a better representation of absorbing aerosols in climate
58 models and remote sensing algorithms (e.g., Samset et al., 2018). In this regard, improving the accuracy of in situ
59 measurements of the spectral aerosol absorption coefficient b_{abs} is fundamental for contributing to robust CRI, MAC and
60 SSA evaluation.

61 The Aethalometer (Hansen et al., 1984; Drinovec et al., 2015) is the most used instrument for routine measurements of
62 the aerosol absorption coefficient in the GAW (Global Atmospheric Watch) and ACTRIS-RI (Aerosol, Clouds, and Trace
63 gases Research Infrastructure; <https://www.actris.eu/>) observational networks (e.g., Laj et al., 2020; Savadkoobi et al.,
64 2023; Rovira et al., 2025), with a long-record of applications in ground-based and airborne intensive field campaigns (e.g.
65 Fialho et al., 2005; Sandradewi et al., 2008; Formenti et al., 2011; Di Biagio et al., 2016; Favez et al., 2021; Ohata et al.,
66 2021) and laboratory experiments (e.g. Weingartner et al., 2003; Baldo et al., 2023; Di Biagio et al., 2019; Kalbermatter
67 et al., 2022).

68 The aethalometer is a filter-based photometer. It measures the light attenuation (ATN) through a filter on which the
69 aerosol is continuously collected at a constant flow rate. The volume absorption coefficient is estimated via the Beer–
70 Bouguer–Lambert law based on the ATN rate of change over the time interval Δt (typically 1–2 minutes). This rate is
71 proportional to the absorbing aerosol concentration and it is also used to calculate an optically-equivalent BC mass
72 concentration (eBC, $\mu\text{g m}^{-3}$) using prescribed instrumental MAC spectral values (Petzold et al., 2013). The aethalometer
73 measurement technique has the advantage of being sensitive to low aerosol signals even for relatively low integration
74 times (e.g., Hansen et al., 1984) and so to be adapted to measurements in environments with variable aerosol loadings.
75 The aethalometer is also easily deployable and provides b_{abs} at seven wavelengths covering the broad range from 370 to
76 950 nm.

77 Despite its operational advantages, the aethalometer measurement is affected by environmental and aerosol-related
78 artefacts that can seriously bias the retrieved absorption coefficient (Arnott et al., 2005; Schmid et al., 2006; Virkkula et
79 al., 2015; Weingartner et al., 2003, hereafter referred as W2003; Collaud Coen et al., 2010, hereafter referred as C2010).
80 These are linked to three causes: 1. the accumulation of particles on the filter that reduces the linearity in the detected
81 attenuation signal, therefore causing an underestimate of the absorption coefficient for increasing aerosol deposition (the



loading effect); 2. the scattering from particles deposited on the filter that contributes to detected attenuation and that causes an overestimation of the absorption (the scattering effect); 3. the multiple scattering by the filter fibers causing an increased optical path and absorption overestimation (the multiple scattering effect).

Aethalometer models commercialized by Magee Scientific have evolved over time to address the known measurement artefacts. Earlier models, such as the AE31, did not include any automatic correction for these effects. Instead, post-processing algorithms and empirical correction factors—extensively studied and developed in the literature—were required to compensate for biases such as loading, scattering, and multiple scattering (Weingartner et al., 2003; Arnott et al., 2006; Bond and Bergstrom, 2006; Collaud Coen et al., 2010; Segura et al., 2014; Backman et al., 2017; Di Biagio et al., 2017; Saturno et al., 2017).

The more recent AE33 model, includes a dual-spot system that automatically compensates for the loading effect in real time (Drinovec et al., 2015). However, even in newer models, the correction for scattering and multiple scattering still relies on the application of a scaling factor, typically referred to as C or C_{ref} . As of today, estimations of the C from various field and laboratory studies have been performed, investigating aerosols of different types and properties and varying ambient conditions (Corbin et al., 2018; Kim et al., 2019; Laing et al., 2020; Valentini et al., 2020; Moschos et al., 2021; Yus-Díez et al., 2021; Bernardoni et al., 2021; Kalbermatter et al., 2022). These studies have reported a wide range of C values, from about 2.26 to 8.26, which translates into significant uncertainty, as b_{abs} is inversely proportional to this factor. This variability remains one of the major challenges in standardizing and comparing absorption measurements across different studies and networks.

As of today, there is still no consensus on the appropriate value of C or its dependence on specific aerosol properties or experimental conditions. The influence of parameters such as particle size, chemical composition, and spectral wavelength on C remains debated. Particle size can lead to bias in the measurement of the absorption coefficient carried out with filter-based instruments (Lack et al., 2009; Nakayama et al., 2010). This dependence is related to the different depth of penetration of particles of different sizes into the filter, as well as to the characteristics of the filter (Hinds, 1999; Huang et al., 2013; Berry et al., 2023). For the aethalometer, particle size has been suggested as a factor that could contribute to the variability of C values across different locations and seasons (Bernardoni et al., 2021; Luoma et al., 2021), although direct observational evidence for this dependence in the aethalometer AE33 remains limited (Drinovec et al., 2022; Yus-Díez et al., 2025). Regarding the composition, previous studies have demonstrated that the optical properties of sampled particles can directly influence aethalometer measurements by altering the amount of scattered light, which the instrument may incorrectly interpret as absorption. An increase in the SSA has been linked in these studies to a corresponding rise in the C values (Schmid et al., 2006; Backman et al., 2017; Yus-Díez et al., 2021). Moreover, very few studies have focused on C estimations for aerosol populations with high fractions of black and brown carbon (BC and BrC), such as those found near combustion sources or in laboratory studies on combustion aerosols.

This uncertainty has practical implications, particularly for international observation networks like ACTRIS RI, which currently recommend the use of a single, wavelength-independent C value. The objective of this study is to improve the characterization of the C parameter for the AE33 aethalometer model, currently the most widely used. Specifically, we investigate its potential dependence on aerosol properties such as particle size, single scattering albedo (SSA), and measurement wavelength. To capture a wide range of conditions, the analysis includes both field data from a mountain observatory with highly variable aerosol loads and properties, and chamber experiments involving combustion-generated soot with varying BC and BrC content under atmospherically relevant conditions.



121 **2 Methods**

122 The C dependencies were investigated through the synergic use of both chamber experiments and observational long term
123 data series. While ambient measurements are valuable for investigating the spatial and temporal variability of C in the
124 real atmosphere, chamber experiments provide a more controlled setting, where variability of multiple variables can be
125 minimized, enabling a clearer understanding of how the C-factor depends on specific particle properties.

126 This section provides description of the experimental setup for field and chamber experiments and description of C factor
127 calculations. A summary of the instruments considered in this study, including deployment details and availability, and
128 measurement uncertainties is provided in Table 1 and Table 2. All volumetric quantities used in the analysis were
129 converted to standard temperature and pressure conditions (STP), assuming 1013.25 mbar and 273.15 K.

130 **2.1 Experimental set-up**

131 **2.1.1 Field measurements at Mt Cimone**

132 Field measurements were carried out at the mountain site of Monte Cimone (CMN, Italy, 44°11'N-10°42'E, 2165 m
133 a.s.l.), located in northern Italy near the Po Valley. The CMN observatory is situated on the summit of the highest
134 mountain in the northern Apennines, and its orographic features allow air masses to arrive from all directions, making it
135 representative of a relatively pristine atmosphere. However, particularly during summer and midday hours, it may be
136 subject to the uplift of pollutants due to planetary boundary layer (PBL) rise and valley breezes (Marinoni et al., 2008;
137 Cristofanelli et al., 2009; Andrews et al., 2011; Cristofanelli et al., 2018). The site is also subject to Saharan dust intrusions
138 (Vogel et al., 2025) and the long-range transport of wildfire emissions throughout the year (Cristofanelli et al., 2009,
139 2024). These diverse conditions affect aerosol properties, including particle size (e.g., following dust transport or new
140 particle formation events; Vogel et al. 2025) as well as their optical and chemical characteristics, influenced by sources
141 such as the Po Valley, wildfires, and dust.

142 The CMN station is part of the World Meteorological Organization's (WMO) Global Atmosphere Watch (GAW) program
143 and high-quality routine measurements of major aerosol properties are conducted in accordance with the ACTRIS-RI
144 guidelines. This study presents measurements collected between July 2020 and November 2022. Aerosols were sampled
145 through a TSP (Total Suspended Particles) inlet, specifically designed for high mountain stations.

146 The spectral absorption coefficient was measured using a dual-spot AE33 aethalometer (RH < 40% ensured by a Nafion®
147 dryer), and complemented by reference absorption techniques: the Multi-Angle Absorption Photometer (MAAP, online,
148 637 nm, Thermo Sci.; Petzold and Schönlinner, 2004) and the Multi-Wavelength Absorption Analyzer (MWAA, offline,
149 5 wavelengths, 375-405-532-635-870 nm, Massabò et al., 2015). The scattering coefficient was measured with an
150 integrating nephelometer (TSI Inc., model 3563, Anderson et al., 1996; Massoli et al., 2009).

151 **2.1.2 Simulation experiments in the CESAM chamber**

152 Chamber experiments were performed in controlled conditions in the 4.2 m³ stainless-steel multi-instrumented CESAM
153 chamber (French acronym for Experimental Multiphasic Atmospheric Simulation Chamber, <https://cesam.cnrs.fr/>; Wang
154 et al., 2011), which has been extensively used in recent years to simulate the formation and aging of different types of
155 aerosols and investigate their physico-chemical and spectral optical properties (Denjean et al., 2015; Di Biagio et al.,
156 2017, 2019; De Haan et al., 2020; Baldo et al., 2023).



The experiments were performed during three campaigns occurred in May 2021, October 2021 and December 2022 and involved primary combustion BC- and BrC-containing soot aerosols. Full detailed description of the setup and data analysis for those experiments is provided in Heuser et al. (2024).

Soot aerosols with varying BC and BrC content were generated by a computer-controlled miniCAST burner (model 6204C, Jing Ltd., Switzerland). The miniCAST is a co-flow diffusion flame generator. It produces soot aerosols (hereafter identified as cast soot, CS) by burning a mixture of propane (C_3H_8), N_2 and oxidation air. Varying the proportions of these gases allows to vary the size, composition and morphology of the generated CS particles (e.g. Moore et al., 2014; Bescond et al., 2016). In this study five different miniCAST operation points were investigated, corresponding to four fuel-lean burning conditions (CS1–CS4) and one fuel-rich condition (CS5) (Table S1). The CS aerosol particles were injected in CESAM via a charcoal denuder to remove volatile organic compounds possibly present in the miniCAST exhaust. After injection in the chamber, the CS was left in suspension to age under different controlled conditions. In this work we only consider experiments in which CS is aged under dry conditions for aging times between 2 and 6 hours.

Between experiments, the chamber was mechanically evacuated and pumped to $3 \cdot 10^{-4}$ mbar for at least a few hours and usually over a full nighttime period. In addition to overnight evacuation, the chamber was manually cleaned at the beginning of each campaign. Background concentrations of aerosols in the chamber were usually less than $0.05 \mu g m^{-3}$ (that is nearly 10^4 times less than the injected CS mass concentration in the chamber reaching up to 60 to $95 \mu g m^{-3}$). The different experimental conditions for chamber experiments are summarized in Table S1 and S2. For the majority of experiments several repetitions are performed to test the reproducibility of results.

The spectral absorption coefficient was measured in CESAM by means of a dual spot aethalometer AE33, complemented by the extinction-minus-scattering (EMS) approach (Onasch et al., 2015; Modini et al., 2021) as reference absorption technique. The extinction coefficient was measured by means of a CAPS PMex instrument (Aerodyne, Massoli et al., 2010) and the scattering coefficient by an integrating nephelometer (TSI Inc., model 3563, Anderson et al., 1996; Massoli et al., 2009).

2.2 Quantification of C factor for the dual spot aethalometer

The aethalometer measures the attenuation coefficient $b_{atn}(\lambda)$ which is proportional to the light attenuation (ATN) rate of change over time. The multiple scattering correction factor C is defined as:

$$C(\lambda) = \frac{b_{atn,LC}(\lambda)}{b_{abs,ref}(\lambda)} \quad (1)$$

where $b_{atn,LC}$ is the attenuation coefficient measured by the aethalometer and corrected for the loading effect based on the AE33 automatic internal algorithm, described in the next section, and $b_{abs,ref}$ is the reference absorption coefficient.

2.2.1 Dual-spot aethalometer loading correction

The model AE33 automatically corrects for the loading effect, through an internal algorithm, by measuring the change in light attenuation in two filter spots, crossed by different air flows, therefore with different aerosol loads. The ATN measurements from the two spots are combined through a set of equations detailed in Drinovec et al. (2015) to provide as output the eBC_{AE33} based on the following formulation:

$$eBC_{AE33}(\lambda) = \frac{S \cdot \left(\frac{\Delta ATN_1(\lambda)}{100} \right)}{F_1(1 - \zeta) \cdot MAC_{AE33}(\lambda) \cdot C_{instr} \cdot (1 - k(\lambda) \cdot ATN_1(\lambda)) \cdot \Delta t} \quad (2)$$



where S is the spot surface area (m^2), ΔATN_1 is the variation of attenuation through the filter spot1 (that is the one with the highest flow rate) in the time interval Δt , F_1 is the flow rate through spot1 ($\text{m}^3\text{min}^{-1}$), ζ is the flow leakage (taking into account lateral flow in the filter matrix), $\text{MAC}_{\text{AE33}}(\lambda)$ is the instrumental mass absorption cross section (18.47, 14.54, 13.14, 11.58, 10.35, 7.77, 7.19 m^2g^{-1} at 370, 470, 520, 590, 660, 880, 950 nm, respectively), and $k(\lambda)$ is a corrective parameter derived by the instrument algorithm to automatically account for the loading effect. As indicated in Eq. (2) the algorithm also accounts for an instrumental multi scattering correction $C_{\text{instr,AE33}}$ (wavelength-independent) for harmonization among aethalometers using different tape materials (quartz, TFE-coated glass; Drinovec et al., 2015). The $C_{\text{instr,AE33}}$ value depends on the filter material and is 1.39 for the for the M8060 filter tape used in this study. Starting from Eq. (2) the spectral loading–corrected attenuation coefficient $b_{\text{atn,LC}}(\lambda)$ is derived from $e\text{BC}_{\text{AE33}}$ data by multiplying for the default instrumental $C_{\text{instr,AE33}}$ and the $\text{MAC}_{\text{AE33}}(\lambda)$ as:

$$b_{\text{atn,LC,AE33}}(\lambda) = e\text{BC}_{\text{AE33}}(\lambda) \cdot \text{MAC}_{\text{AE33}}(\lambda) \cdot C_{\text{instr,AE33}} \quad (3)$$

As previously noted by Cuesta-Mosquera et al. (2021), the automatic AE33 loading correction method has limitations, particularly around filter changes, potentially introducing biases. These limitations are particularly critical when absorbing aerosol concentration is high, filter changes frequent (tens of minutes-few hours), and experiment durations relatively short. At CMN, where the concentration of absorbing species is typically low ($0.2 \mu\text{g m}^{-3}$), the filter changes occur after several hours or days. Conversely, for chamber experiments, the higher soot concentration leads to frequent filter changes (tens of minutes-few hours). In the present analysis, both for field measurements and chamber experiments, the internal correction automatically applied by the instrument was utilized. For field measurements, the $b_{\text{atn,LC}}(\lambda)$ values obtained at 1-minute resolution from the $e\text{BC}(\lambda)$ values provided by the instrument were averaged over one hour. Conversely chamber data, for which experiment duration is limited, were analysed at 1-min resolution.

A detailed discussion on the effect of high soot concentrations on the loading correction for the AE33 $b_{\text{atn,LC}}(\lambda)$ calculation and C evaluation for chamber experiments is provided in the Supplementary Information (Text S1 and S2).

2.2.2 Reference absorption coefficient at CMN: filter-based MAAP and MWAA

The MAAP and the MWAA are the filter-based reference instruments used at CMN. The MAAP is based on the simultaneous measure of both the reflected and the transmitted light of aerosols embedded in a filter. An algorithm based on the Mie theory and the two stream approximation is then used to convert these signals in values of SSA_{PF} and optical thickness ($\tau_{\text{PF}} = \ln(T_{\text{PF}})$) of the particle–filter (PF) system. These parameters allow to retrieve the aerosol absorption coefficient using the equation:

$$b_{\text{abs,ref}} = \frac{S}{V} \text{ABS} = -\frac{S}{V} (1 - \text{SSA}_{\text{PF}}) \ln(T_{\text{PF}}) \quad (4)$$

where S is the spot surface area (m^2) of collection and V the sampled volume of air (m^3). The basic principle of the MWAA technique is based on the MAAP concept. However, while the MAAP is a field–deployable instrument working at a single wavelength (637 nm), the MWAA is a laboratory–based setup that extends the principle of the MAAP to 5 wavelengths and analyze filter aerosol samples. Because of their different nature, the MAAP is a high resolution instrument (with observations typically every minute) while the MWAA integrates observations across an aerosol sampling period that can be variable depending on the concentrations (minutes to hours).

The MAAP is routinely measuring at the CMN site collecting data of $b_{\text{abs,ref}}$ at 637 nm at 1-min time resolution. Data measured in the period from July 2020 to November 2022 are considered in this study. The MWAA technique was instead



used to measure the $b_{\text{abs,ref}}$ at 5 different wavelengths on 43 samples collected every 24 hours by the MAAP at CMN in the period September-October 2022.

The $b_{\text{abs,ref}}$ at 637 nm measured by the MAAP were averaged over the same 1-h step of the AE33 and used to estimate the C at 637 nm based on Eq. (1). The AE33 $b_{\text{atn,L,C}}$ data at 637 nm were interpolated at 637 nm using the absorption Ångström exponent (AAE) calculated as the power-law fit of $b_{\text{atn,L,C}}(\lambda)$ vs the wavelength ($b_{\text{atn,L,C}} \sim \lambda^{-\text{AAE}}$).

The $b_{\text{abs,ref}}(\lambda)$ measured by the MWAA was used to study the spectral dependence of C. Values of C were calculated at the $7-\lambda$ of the aethalometer, averaging $b_{\text{atn,L,C}}(\lambda)$ over the same 24 hours of MWAA samples and interpolating the $b_{\text{abs,ref}}(\lambda)$ at the AE33 wavelengths ($b_{\text{abs,ref}} \sim \lambda^{-\text{AAE}}$).

2.2.3 Reference absorption coefficient at CESAM: extinction-minus-scattering approach

The EMS approach is considered as reference absorption technique for chamber experiments. This method involves the simultaneous measurements of both the extinction (b_{ext}) and scattering coefficient (b_{sca}) and the absorption coefficient is obtained as the difference of the two. When applied in the field to predominantly scattering samples, this technique is affected by high level of uncertainty as discussed in Modini et al. (2021). However, it can be successfully used as a good standard in laboratory experiments with high absorption signals. Validation of the methodology is provided in Heuser et al. (2024). In this study the extinction coefficient at 630 nm was measured by means of a CAPS PMex instrument (Aerodyne, Massoli et al., 2010). Extinction coefficient measured from the CAPS PMex does not require further adjustments. The scattering coefficient at 450, 550, and 700 nm was measured by an integrating nephelometer (TSI Inc., model 3563, Anderson et al., 1996). The nephelometer b_{sca} needs to be corrected for truncation, in order to compensate for the limited field of view of the instrument. The truncation correction was calculated using the Massoli et al. (2009) approach adapted to highly absorbing aerosols as those probed in chamber experiments, as discussed in Heuser et al. (2024). Assumptions on the real refractive index are required in the Massoli et al. (2009) calculation. For the different experiments considered in this study the real index was set at $n=1.9$, based on the proposed CRI for fresh BC by Bond and Bergstrom (2006). A sensitivity test was performed to investigate the potential error caused by this assumption. Changes in the corrected scattering signal for a range of likely real parts was found to be 4%.

The truncation-corrected b_{sca} values were interpolated at 630 nm based on the Scattering Ångström Exponent (SAE) calculated as the power-law fit of b_{sca} vs the wavelength ($b_{\text{sca}} \sim \lambda^{-\text{SAE}}$). The b_{abs} at 630 nm was calculated at 1-min resolution as the difference of the CAPS-PMex b_{ext} and the nephelometer b_{sca} . The C values at 630 nm were derived at 1-minute resolution and then averaged over each aethalometer filter spot.

2.3 Ancillary measurements

2.3.1 Single scattering albedo (SSA)

The aerosol SSA was calculated at 637 nm and 1-hour resolution at CMN and at 630 nm at 1-minute resolution for chamber experiments, as:

$$\text{SSA} = \frac{b_{\text{sca}}}{b_{\text{ext}}} \quad (5)$$

The b_{sca} was measured at 450 nm, 550 nm, and 700 nm by the TSI nephelometer both in field and in the chamber. At CMN the nephelometer data were corrected for truncation effects following the method of Anderson and Ogren (1998) and extrapolated at 637 nm as ($b_{\text{sca}} \sim \lambda^{-\text{SAE}}$). Only measurements taken at relative humidity levels below 40% were



considered. The b_{ext} in Eq. (5) was calculated as $(b_{\text{sca}} + b_{\text{abs,ref}})$ at CMN, while retrieved from CAPS PMex data in the chamber.

2.3.2 Particle size distribution

The particle number size distribution ($dN/d\log D_m$; D_m , mobility diameter), in the range of diameters from 10 to 800 nm, was measured at CMN by using a scanning particle mobility sizer (SMPS-TROPOS), operating at 5-minutes resolution and at $5/1 \text{ l min}^{-1}$ sheath/aerosol flow rates. In chamber experiments the particle number size distribution, was instead measured in the range of diameters from 19.5 to 881.7 nm, by using a scanning particle mobility sizer (TSI SMPS) consisting in an ^{85}Kr neutralizer, a Differential Mobility Analyzer (DMA, model 3080, TSI Inc.), and a Condensation Particle Counter (CPC, model 3772, TSI Inc.), operated at $2.0/0.2 \text{ l min}^{-1}$ sheath/aerosol flow rates, and at a time resolution of 3 minutes. Measurements were corrected for diffusion losses and multiple charge effects with the instrument software. The size distribution measured by the SMPS was used to derive the geometric mean diameter ($D_{m,\text{geo}}$) through the following equation:

$$\ln(D_{m,\text{geo}}) = \frac{\sum_{i=m}^n \Delta N_i \cdot \ln(d_i)}{N} \quad (6)$$

where d_i is the midpoint diameter for size channel i , N is the total concentration, ΔN_i is the particle concentration within channel i , m is the first channel, and n is the last channel. The equation was applied to hourly averaged size distributions at CMN and to both 3-minutes size distributions and size distribution averaged on each filter spot of the aethalometer in chamber experiments. The uncertainty associated to the geometric mean diameter was the geometric standard deviation. To notice that in the field the size distribution is multi-modal and include both absorbing and non-absorbing particles, in chamber experiments they were mono-modal and including only absorbing aerosols.

Table 1: Datasets and optical instruments deployed for field observations at Cimone (CMN) and CESAM chamber experiments used in the present analysis.

Site	Period	Optical instrumentation
CMN	July 2020 - November 2022	AE33, MAAP, nephelometer
	September - October 2022	AE33, MAAP, MWAA, nephelometer
	May 2021	
CESAM	October 2021	AE33, CAPS Pmex, nephelometer
	December 2022	



289

290 **Table 2:** Technical details of the instruments used in the present analysis. The sampling flow rate and temporal resolution of data
291 acquisition for field and chamber deployments are provided.

Instrument	Wavelengths (nm)	Percent uncertainty	Reference	Flow rate (l min ⁻¹)		Temporal resolution		Size range (nm)	
				CMN	CESAM	CMN	CESAM	CMN	CESAM
Aethalometer (model AE33, Magee Sci.)	370, 470, 520, 590, 660, 880, 950	± 24 %	Drinovec et al. (2015) Cuesta-Mosquera et al. (2021)	5	2	1 min	1 min	–	–
Multi-Angle Absorption Photometer MAAP (model 5012, Thermo Sci.)	637	±12%	Petzold and Schönlinner (2004) Petzold et al. (2005)	17	–	1 min	–	–	–
Multi-Wavelength Absorption Analyzer (MWAA, custom-made)	375, 405, 532, 635, 850	± 3-20 %	(Massabo et al., 2013)	–	–	24 hours	–	–	–
Nephelometer (model 3563, TSI Inc.)	450, 550, 700	± 8 %	Anderson (1996) Anderson and Ogren (1998) Massoli et al. (2009)	35	2	1 min	1 sec	–	–
Cavity Attenuated Phase Shift Extinction (CAPS PMex, Aerodyne)	450, 630	± 6%	Massoli et al. (2010)	0.85	–	–	1 sec	–	–
SMPS	–	–	(Wiedensohler et al., 2012)	5	2	5 min	3 min	10-800	19.5-881.7

292



293 3 Results

294 3.1 Investigating C dependence on particle properties with chamber experiments

295 The experiments in the CESAM simulation chamber, presented in this study, were designed to investigate the specific
 296 dependence of the C-factor on the chemical and physical properties of highly absorbing BC-containing soot particles. The
 297 five different cast soot (CS) studied in the present work correspond to four fuel–lean burning conditions (CS1–CS4) and
 298 one fuel–rich condition (CS5) leading to particles with a decreasing EC/TC ratio (0.79 ± 0.11 for CS1 to 0.00 ± 0.22 for
 299 CS5) and decreasing number median diameter (from an average of 145 ± 12 nm for CS1 to 79 ± 2 nm for CS5, expressed
 300 as mobility diameter (Heuser et al., 2024).

301 3.1.1 Average chamber C value and the role of loading correction

302 The average values of C and their corresponding uncertainties for each experimental condition in the chamber are
 303 summarized in Table 3. These values range from 2.89 ± 0.03 to 3.9 ± 0.06 , with the highest values corresponding to CS5,
 304 which is characterized by a higher organic content and smaller particle sizes. The lowest values correspond to CS1, which
 305 has a higher content of elemental carbon and larger particle sizes. The C values obtained for soot in the chamber
 306 experiments are similar, considering the uncertainties, to the values reported in other studies from the urban site of Milan
 307 (Bernardoni et al., 2021; Ferrero et al., 2021) and laboratory experiments using soot generated with a miniCAST burner
 308 (Kalbermatter et al., 2022).

309 Due to the high concentration of absorbing soot, the possible dependence of the retrieved C on the loading correction
 310 scheme was also evaluated. Indeed, in case of high absorbing aerosols concentration and frequent filter changes, the
 311 internal AE33 correction can provide uncertain results. The time variability of the $b_{\text{am,LC}}$ may in some cases not to follow
 312 the same decreasing trend over time as the reference measurement. However, it showed a steeper decline before and after
 313 the filter change, with a more rapid decrease in these points, making the trend appear more abrupt and also discontinuous
 314 around the filter transition. In these cases, the AE33 data can be re-corrected for loading effect. With this aim, the AE33
 315 can be treated like a single-spot aethalometer and the loading correction schemes from W2003 or C2010 be applied. In
 316 the present analysis we tested the impact of different loading correction schemes on C retrieval and found that the method
 317 applied to correct loading can introduce differences of maximum 30% in the average values. Despite not impacting the
 318 conclusion of the present study, the role of loading effect and correction scheme on retrieved C and b_{abs} should be taken
 319 into consideration. A detailed discussion of this specific analysis is provided in Supplementary Information.

320

321 **Table 3:** Average C values for each soot type (CS1–CS5) and associated particles properties. In particular, the average geometric mean
 322 diameter ($D_{\text{m,geo}}$), absorption coefficient b_{abs} and single scattering albedo (SSA). These values were derived averaging the results
 323 obtained for all aethalometer filter spots corresponding to the same CS type. Values obtained in this study are shown together with the
 324 ratio between elemental and total carbon mass concentration (EC/TC) and the Absorption Ångström Exponent (AAE) derived in Heuser
 325 et al. (2024).

	C (630 nm) (this study)	$D_{\text{m,geo}}$ [nm] (this study)	b_{abs} [Mm^{-1}] (this study)	SSA (630 nm) (this study)	AAE (Heuser et al., 2024)	EC/TC (Heuser et al., 2024)
CS1	2.89 ± 0.03	169.9 ± 1.7	450 ± 30	0.08 ± 0.01	1.27 ± 0.13	0.79 ± 0.11
CS2	3.00 ± 0.03	152.7 ± 1.6	179 ± 11	0.09 ± 0.01	1.36 ± 0.21	0.73 ± 0.08
CS3	2.96 ± 0.03	171.3 ± 1.7	400 ± 30	0.09 ± 0.01	1.59 ± 0.22	0.67 ± 0.09
CS4	2.99 ± 0.03	146.2 ± 1.6	59 ± 4	0.08 ± 0.01	1.88 ± 0.31	0.53 ± 0.13
CS5	3.90 ± 0.06	101.2 ± 1.5	63 ± 6	0.29 ± 0.03	3.79 ± 0.33	0.00 ± 0.22

326



3.1.2 C dependence on soot microphysical properties: the dominating role of size

The C values at 630 nm averaged over each aethalometer filter spot interval were analyzed to identify the dependence on average properties of the particles collected on the filter. These properties include particle size, absorption coefficient, SSA, and chemical composition (measured as the EC/TC ratio). The results are summarized in Figure 1. The analysis shows that the C factor increases from 2.75 to 4.45 as the mean particle diameter of BC generated particles decreases from 225.2 nm to 67.8 nm. This is particularly evident for particles smaller than 120 nm, while at larger sizes the trend is not significant when considering the associated uncertainties. The points with the highest C values and smallest sizes correspond to experiments involving CS5 particles. These particles are not only smaller but also differ in composition, with a negligible fraction of EC in spite of dominating OC composition. This compositional difference significantly affects the optical properties, increasing the SSA from 0.05-0.09 for C1-CS4 to 0.27 for CS5 at 630 nm and the AAE from around 1.27-1.88 to 3.79 (Heuser et al., 2024). However, focusing on a subset of points with limited size variability (120-160 nm, highlighted in the grey box), it becomes evident that at similar diameters, C values are comparable for CS5 particles and CS1-CS4 particles. Moreover, for CS5 particles, C increases significantly from 3.15 to 4.45 as the mean diameter decreases from 132.9 nm to 67.8 nm. This suggests that the size is the dominant factor impacting the C variability in these experiments. This result is consistent with the impact of particle size on absorption measurements in filter-based instruments, as previously observed for the aethalometer (Drinovec et al., 2022; Yus-Díez et al., 2025) and other instruments (Lack et al., 2009; Moteki et al., 2010; Nakayama et al., 2010). Small particles, which can penetrate more deeply into the filter matrix and exhibit more isotropic scattering patterns, may enhance the multiple scattering effect, resulting in a greater overestimation of true absorption by the aethalometer. The variability in SSA, which was observed to influence the C factor at high values in previous works (Yus-Díez et al., 2021), appears to have a limited impact in this low-SSA regime. The C-size dependence was observed for any loading correction scheme applied as shown in Supplementary Information.

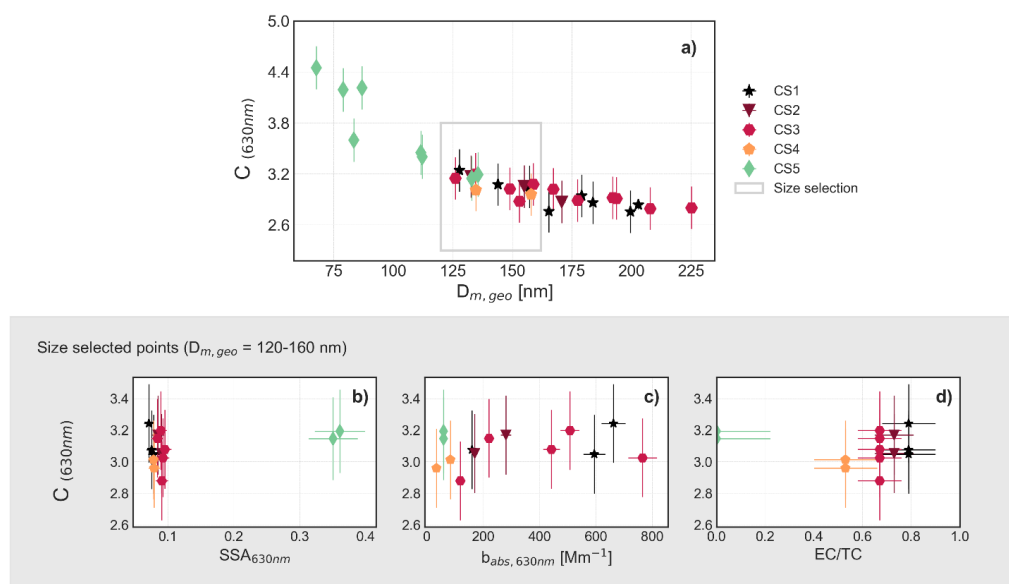


Figure 1: C dependence on particle size in laboratory studies measuring the properties of different freshly emitted particles (CS1-CS5). The top panel shows the C dependence on the size ($D_{m,geo}$). The bottom panels show the dependence of C values with the SSA, b_{abs} (measured by the EMS technique) and the EC/TC ratio, in experiments where the diameter was in the range 120-160 nm (grey rectangle in the top panel).



3.2 Ambient variability of the C factor

In this section, the results obtained from field measurements on the environmental variability of the correction factor C are presented. These results provide insights into how C values fluctuate across different seasons and aerosol properties.

3.2.1 Average ambient C value and seasonal variability

The variability of the C factor at a wavelength of 637 nm was analysed on hourly base at the CMN site. The average C value over the period July 2020 - November 2022 is 2.35 with a standard deviation of 0.58. This value is comparable, within the combined uncertainties of MAAP and AE33 (27%), with the 2.45 value suggested by the ACTRIS guidelines for M8060 filter tape (obtained as the product of a C_{instr} factor (1.39) and the harmonization factor H^* (1.76); <https://www.actris-ecac.eu/particle-light-absorption.html>). This value is also in line, even if slightly lower, to mean values reported in other studies conducted at various sites (urban, background and mountain sites) using the same reference techniques (MAAP, MWAA) and filter tape, which range between 2.44 and 2.66 (Moschos et al., 2021; Valentini et al., 2020; Yus-Díez et al., 2021). However, when considering the range of values reported in the literature, which consider different reference techniques for measuring absorption (e.g., two-wavelength Photothermal Aerosol Absorption Monitor PTAAM-2 λ , and the Cavity Attenuated Phase Shift CAPS SSA), various AE33 filter types, different wavelengths, and diverse environmental or experimental conditions (such as chamber studies with artificially generated soot or emissions from heavy fuel oil), the reported values can vary significantly from 2.26 to 8.26 (Corbin et al., 2018; Laing et al., 2020; Ferrero et al., 2021; Bernardoni et al., 2021; Kalbermatter et al., 2022). The averaged ambient value was also 23-66% lower compared to the average values obtained for freshly emitted soot in the chamber experiments. This difference could be due to the use of different reference method for measuring absorption or it could reflect differences in particle composition.

Figure 2 and Table 4 summarize the seasonal variability of C values at the CMN site. Throughout the year, C mean ranged from a minimum of 2.30 in spring to a maximum of 2.41 in winter, indicating a slight increase in the colder months. At the same time, the coldest seasons (winter and autumn), also showed the greatest variability, resulting in the highest standard deviations (0.7-0.8). The difference between the seasons, although significant based on the Kolmogorov-Smirnov test, was small compared to the combined instrumental uncertainty of the MAAP and the AE33.

Nonetheless, the seasonal variability observed at CMN was smaller in magnitude and opposite in trend compared to the biogenic-dominated site in the Finnish boreal forest (Luoma et al., 2021) and to the mountain site of Montsec d'Ares (Spain, 1570 m a.s.l.; Yus-Díez et al., 2021). In these previous studies, seasonal variability was explained as a result of dependence on optical (SSA; Yus-Díez et al., 2021) and microphysical (diameter; Luoma et al., 2021) properties, as well as aerosol composition (presence of dust; Yus-Díez et al., 2021). Hence, we addressed the dependency of C at CMN on particles properties, concentration and wavelength.

3.2.2 Lower limit of b_{abs} for C determination

One of the most critical challenges in determining C at a remote site like CMN, where aerosol concentrations are low, is that the absorption coefficient (b_{abs}) often approaches the detection limits of the instruments used. At very low concentrations, measurements are increasingly affected by instrumental noise, compromising the reliability of the resulting C values. To set a reasonable threshold for investigating the dependence of C on particle properties—while



avoiding the exclusion of a substantial portion of the dataset—we first examined how C varies with the absorption coefficient (b_{abs}) measured with the MAAP, and assessed the influence of low b_{abs} values on the C estimates.

Figure 3 shows the dependence of C on b_{abs} , with higher C values observed at decreasing b_{abs} . In particular, C more frequently reaches values of 10 or higher when b_{abs} falls below 0.06 Mm^{-1} , although this condition accounts for less than 3% of the dataset. These extreme values can significantly affect the median C (Figure 3), and are more commonly observed during winter and autumn (Table 4) seasons less influenced by anthropogenic emissions from the Po Valley (Marinoni et al., 2008). At such low b_{abs} levels—close to or below the detection limits of both the MAAP and AE33—the signal becomes increasingly dominated by instrumental noise, undermining the reliability of the computed C values (Cuesta-Mosquera et al., 2021). This likely explains both the higher standard deviation observed in winter and the unusually high C values recorded during that season. For this reason, data points where b_{abs} is below 0.06 Mm^{-1} were excluded from subsequent analyses.

Table 4: The mean and standard deviation of C and b_{abs} for each season.

	Winter	Spring	Summer	Autumn	Whole
C					
Mean (SD)	2.40 (0.80)	2.30 (0.45)	2.32 (0.35)	2.41 (0.70)	2.35 (0.58)
$b_{\text{abs}} [\text{Mm}^{-1}]$					
Mean (SD)	0.77 (1.06)	1.49 (1.26)	1.89 (1.08)	1.08 (1.19)	1.36 (1.23)

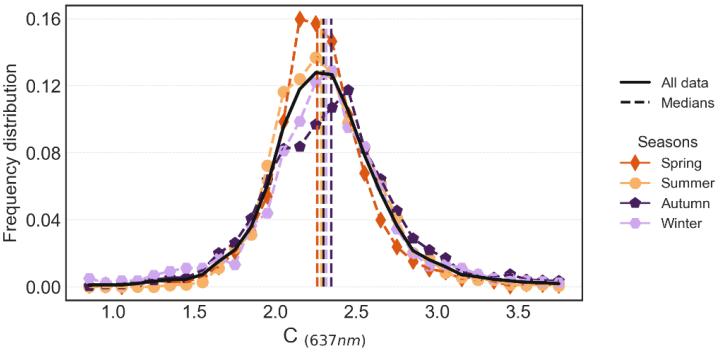


Figure 2: Histograms representing hourly averaged C values frequency distribution at 637 nm for the period July 2020 – November 2022 at CMN. The black line represents the entire period, the coloured histograms correspond to each season in the analysed period. The median values corresponding to each season are also represented as dashed vertical lines. The MAAP was used as reference technique for measuring the absorption coefficient.

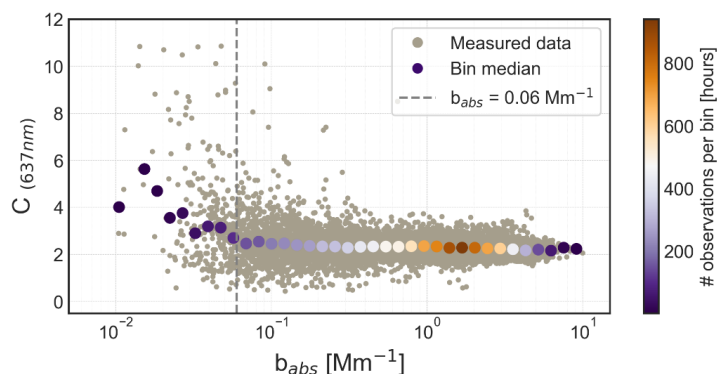


Figure 3: Scatterplot of hourly averaged C values at 637 nm as a function of the corresponding b_{abs} values measured at CMN. The reference technique used to measure the absorption coefficient is the MAAP. Bigger dots are used to represent the median C values in bins of b_{abs} .

3.2.3 C factor increase at high SSA

Previous studies have demonstrated that the optical properties of sampled particles can directly influence aethalometer measurements by altering the amount of scattered light, which the instrument may incorrectly interpret as absorption. An increase in the SSA has been linked in these studies to a corresponding rise in the C values (Schmid et al., 2006; Backman et al., 2017; Yus-Díez et al., 2021).

During the period considered in this study, the SSA at 637 nm varied between 0.6 and 1. Here, the C values are binned to the SSA values (Figure 4). The number of bins was chosen using the ‘auto’ mode of the `numpy histogram_bin_edge` function (python). This function selects as best number of bins, the highest value between those obtained with the Freedman and Diaconis, (1981) or the Sturges, (1926) criteria. For each bin, the median C and the corresponding 25th and 75th percentiles were derived.

At CMN, C remained relatively constant for SSA values below 0.90. It increased slowly for values between 0.90 and 0.94, while a more significant variability was observed for SSA higher than 0.94 (Figure 4). This trend aligns with observations in other studies, where C becomes higher at higher SSA values due to an increase in the multiple scattering between particles and filter fibers and a reduced signal-to-noise ratio in low-absorption regimes (Schmid et al., 2006; Yus-Díez et al., 2021). The SSA- C relationship was fitted using the cross-sensitivity to scattering law proposed by Schmid et al. (2006) and applied in Yus-Díez et al. (2021) as:

$$C = C_f + m_s \left(\frac{SSA}{1 - SSA} \right) \quad (7)$$

Compared to the results presented in Yus-Díez et al. (2021) for another mountaintop site, this curve shows a pronounced increase only at higher SSA values. The fitted curve closely matches the data up to a SSA of 0.97, becoming less representative at higher SSA. The deviation from the expected curve appears to be linked to the occurrence of strong dust events during the two-year period. In fact, over 80% of the hours with SSA values above 0.97 and C values below the mean of 2.3 correspond to days identified as dust-affected, characterized by coarse PM mass concentrations exceeding 37 $\mu\text{g}/\text{m}^3$, according to Vogel et al. (2025). The median C during these days is 2.0, suggesting a decrease in C during dust



events, likely related to the increased presence of coarse particles collected on the filter, even at high SSA values. This decrease is consistent with the findings of Di Biagio et al. (2017), who reported lower C values for the AE31 when comparing measurements of ambient air and mineral dust particles.

These results highlight the importance of carefully selecting appropriate correction factors. Under conditions of high SSA, absorption is typically minimal and may approach the detection limits of the instruments, increasing uncertainty in C estimation. Moreover, part of the variability at high SSA values may arise from changes in aerosol properties, such as the increased presence of coarse particles during dust events. Finally, the discrepancies observed in the fitted curves between different sites, underscore the complexity and site-specific nature of C behaviour, particularly under clean or dust-influenced conditions.

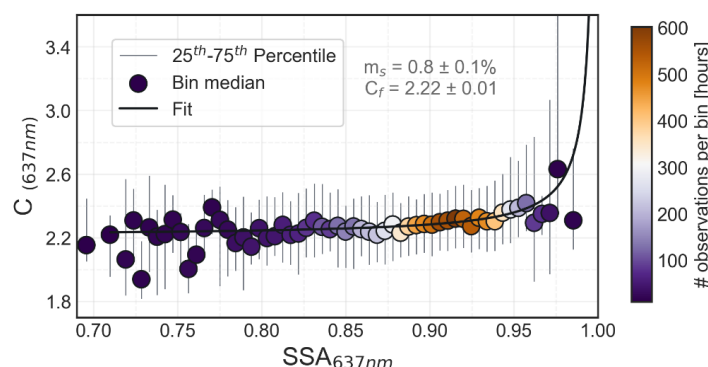


Figure 4: C (637 nm) dependence on the SSA (derived at 637 nm combining MAAP and nephelometer). Reference absorption instrument: MAAP. Dots represent the mean values in each SSA bin, the gray lines the 25th and 75th percentile. The dots colours represent the number of observations used in each bin for calculating the mean and the curve is the fitted curve obtained using Yus-Díez et al. (2021) relation.

3.2.4 C factor increase with decreasing particles size

Previous studies have suggested a possible influence of particle size on the C value (Bernardoni et al., 2021, Luoma et al., 2021, Drinovec et al., 2022; Yus-Díez et al., 2025). A clear relationship between C and the size of freshly generated soot, has also been observed in this study through chamber experiments. In this section, we investigate how C at 637 nm varies with particle size under ambient atmospheric conditions, where isolating the effect of a specific property is more challenging. The aim is to assess whether particle size continues to play a significant role in such complex environments.

During the period studied at CMN, the hourly geometric mean diameter ($D_{m,geo}$) of total aerosol particles ranged from 19 to 173 nm. The analysis of C as a function of particle size revealed a slight (within 15%) C increase as $D_{m,geo}$ decreases (Figure 5), not only observed in the median C values but also for the 25th and 75th percentiles. This analysis was performed by binning C values by particle size ($D_{m,geo}$) and then calculating the median and percentiles in each bin, using the same approach applied for the SSA.



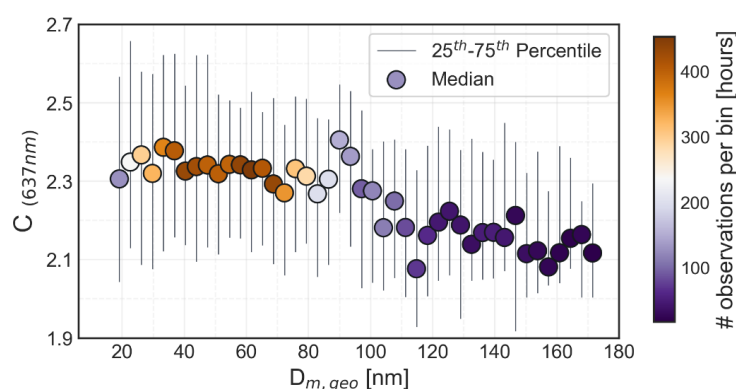
475 This trend is in line with the results obtained from chamber experiments and previous studies (Nakayama et al., 2010;
476 Drinovec et al., 2022; Yus-Díez et al., 2025), but small compared to the instrumental uncertainties. However, it could
477 cause more significant bias in the individual hourly values and actually be one of the causes of the observed variability
478 of C at different sites and seasons.

479

480 Moreover, the C increase is less pronounced than what was observed in chamber experiments (over 60%). This difference
481 may be due to the distinct properties of the particles studied—only absorbing in the chamber and mixed in ambient air—
482 as well as differences in reference measurement techniques. The MAAP, being a filter-based instrument, may be affected
483 as well by particle stratification, making its radiative transfer model an approximation potentially biased, as discussed by
484 Moteki et al. (2010).

485

486



487

488 **Figure 5:** C (637 nm) dependence on the geometric mean diameter $D_{m,geo}$. Reference absorption instrument: MAAP. Dots represent
489 the mean values in each $D_{m,geo}$ bin, the gray lines the 25th and 75th percentile. The dots colours represent the number of observations
490 used in each bin for calculating the median.

491

492 3.2.5 Absence of spectral dependence

493 Figure 6 shows the spectral dependence of C at CMN for observations between September and October 2022, with 43
494 filters collected. The mean C values range from 2.38 ± 0.62 at 470 nm to 2.13 ± 0.60 at 880 nm (Table 5). A statistical
495 Kolmogorov-Smirnov test was applied to quantify the significance of the spectral dependence, and a potentially
496 significant distinction was observed between the 470 nm and 880 nm mean C values (p -value = 0.042). However, for all
497 other wavelength pairs, the test yielded $p > 0.05$, indicating no statistically significant differences, and that despite the
498 high variability in the data, with standard deviations reaching 0.63. Since the overall precision of the AE33 is not
499 wavelength-dependent (Cuesta-Mosquera et al., 2021), all wavelength-dependent C values reported in this study fall
500 within the relative error of $\pm 31\%$, obtained combining the AE33 and MWAA uncertainties.

501

502 Limited studies have investigated the multi-wavelength absorption reference methods for both models of the
503 aethalometer. For the AE31 model, Bernardoni et al. (2021) and Ferrero et al. (2021) did not observe a notable wavelength
504 dependence of the C factor, although they found that applying a wavelength-dependent C correction improved the
505 agreement in the measured absorption coefficient for both AE31 and AE33. In contrast, for the AE33 model, neither



Bernardoni et al. (2021) nor Ferrero et al. (2021) detected significant wavelength dependence after accounting for uncertainties. However, Moschos et al. (2021) reported a decreasing trend in the C factor from 2.5 at 370 nm to 2.3 at 880 nm in Swiss background conditions. Moreover, Yus-Díez et al. (2021) found no significant wavelength dependence, except for aged aerosols, where they observed an increasing C value with wavelength, ranging from 3.47 to 4.03.

Table 5: Mean and standard deviation (SD) of C values for each aethalometer wavelength at CMN. The MWAA was used as reference instrument for the absorption coefficient.

	370 nm	470 nm	520 nm	590 nm	660 nm	880 nm	950 nm
Mean	2.24	2.38	2.29	2.24	2.31	2.13	2.18
(SD)	(0.58)	(0.62)	(0.58)	(0.58)	(0.63)	(0.60)	(0.63)

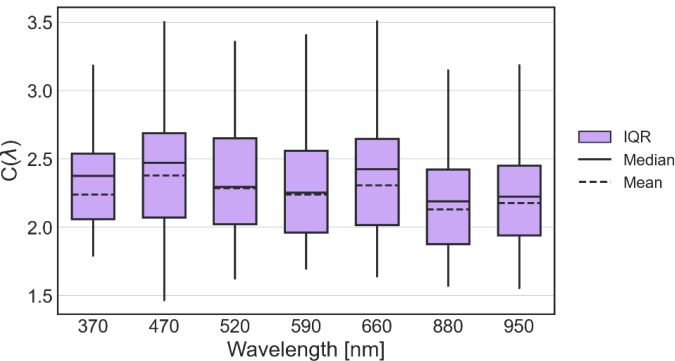


Figure 6: Boxplots describing the statistics of C values derived at each aethalometer wavelength, the 25th – 75th percentile range (IQR), the mean and median are reported. The MWAA was used as the reference technique for measuring the absorption coefficient.

4 Conclusions

In this work we studied the role of aerosol properties on the variability of the multiple scattering correction factor C for the dual-spot aethalometer AE33. For this, we combined data from a long term series in a mountaintop station in northern Italy at Monte Cimone, CMN, and from multiple experiments on laboratory-generated soot at the CESAM simulation chamber. We calculated the C factor comparing the attenuation coefficient measured by the AE33 with the absorption coefficient measured with independent techniques: the MAAP and MWAA at CMN, and the extinction-minus-scattering in chamber experiments.

The C factor obtained by chamber experiments ranged from 2.89 to 3.9 at 630 nm, the highest values corresponding to higher organic content and smaller particle sizes, while the lowest values corresponding to a higher content of elemental carbon and larger particle sizes. The possible dependence of the retrieved C on the loading correction scheme applied was also evaluated and quantified in max 30% of difference in the averaged values.

We found an averaged C factor at 637 nm of 2.35 ± 0.58 at CMN. This value shows a slight seasonal variability with higher values in winter than in summer, difficult to associate to specific particle properties and mainly driven by the



impact on C of the very low signal-to-noise ratio of the absorption coefficient, causing very high C values at low b_{abs} ($<0.06 \text{ Mm}^{-1}$). This was significant particularly at very high SSA values (>0.94), where an impact of the low signal-to-noise ratio of the absorption coefficient cannot be excluded. Moreover, part of the variability at high SSA values was influenced by changes in aerosol properties, such as the increased presence of coarse particles during dust events. We studied also the C spectral dependence finding no evidence of a variability of C within the 370-950 nm spectral range.

The present analysis evidences a dependence of C to particle size. This dependence was small (within 15%) in ambient conditions for mostly scattering aerosols, while it was more pronounced ($>60\%$) in chamber experiments measuring only soot particles and using a non-filter based technique as reference for the absorption coefficient. This dependence observed previously for filter based instruments could explain part of the C factor variability in literature and should be investigated deeply to improve the accuracy of absorption coefficient measurements in international research infrastructures.

5 Appendix

Table A1. List of digital object identifier (DOI) for the CESAM chamber experimental data supporting the findings of this study. Those data are available through the Database of Atmospheric Simulation Chamber Studies (DASCS) of the EUROCHAMP Data Centre (<https://data.eurochamp.org/data-access/chamber-experiments/>).

Cast Soot Type (Date of experiment)	Dataset DOI reference in the EUROCHAMP Data Centre
CS1 (23/02/2021)	https://doi.org/10.25326/8KVR-AA70
CS1 (24/02/2021)	https://doi.org/10.25326/M24W-V933
CS1 (19/10/2021)	https://doi.org/10.25326/5144-DY86
CS1 (12/12/2022)	https://doi.org/10.25326/2BD3-Q151
CS1 (14/12/2022)	https://doi.org/10.25326/9G66-MG61
CS1 (15/12/2022)	https://doi.org/10.25326/XJKP-JD08
CS1 (16/12/2022)	https://doi.org/10.25326/6030-BD74
CS2 (20/10/2021)	https://doi.org/10.25326/ET9M-7H20
CS3 (26/10/2021)	https://doi.org/10.25326/0HMW-HM76
CS3 (06/12/2022)	https://doi.org/10.25326/T145-0S52
CS3 (07/12/2022)	https://doi.org/10.25326/9TR7-BB18
CS4 (22/10/2021)	https://doi.org/10.25326/VPM3-3W86
CS5 (28/05/2021)	https://doi.org/10.25326/BGCT-4J45
CS5 (21/10/2021)	https://doi.org/10.25326/34DX-YJ98
CS5 (08/12/2022)	https://doi.org/10.25326/FWN3-A342
CS5 (09/12/2022)	https://doi.org/10.25326/6M6N-8P33

6 Open Research / Data availability

The CESAM data used in this study are available through the Database of Atmospheric Simulation Chamber Studies (DASCS) of the EUROCHAMP Data Centre (<https://data.eurochamp.org/data-access/chamber-experiments/>) with the identifiers listed in Appendix Table A1. The CMN database is available through ACTRIS DC (EBAS/NILU).

7 Competing interests

The authors declare that they have no competing interests.



557 8 Author contributions

558 LR, AM and CDB conceived the study and discussed the results. LR, AM, MM took care of field measurements. JH and
559 LR conducted the CESAM experiments with contributions by CDB, MC, AB, EP, AM, JY, CY, MZ, PF, BPV, and JFD.
560 DM, TI and VV performed the MWAA measurements. LR performed the full data analysis under the supervision of MZ,
561 AM and CDB and with contributions from JH, and MM. CDB contributed to funding acquisition and project
562 administration for CESAM experiments. LR, MZ, AM and CDB wrote the manuscript. All authors reviewed and
563 commented on the paper.

564 9 Acknowledgements

565 The CNRS-INSU is gratefully acknowledged for supporting the CESAM chamber as a national facility included in the
566 ACTRIS-France Research Infrastructure as well as AERIS (<https://www.aeris-data.fr/>) for curing and distributing the data
567 through the EUROCHAMP Data Center (<https://data.eurochamp.org/>). We thank ACTRIS-Italy for supporting
568 measurements at Monte Cimone, carried out within ACTRIS Research infrastructure (ESFRI).

569 10 Funding

570 This work has received funding from the TNA activity of the European Union's Horizon 2020 research and innovation
571 programme through the EUROCHAMP-2020 Infrastructure Activity under grant agreement No 730997. This study has
572 been supported by the French National Research Agency (ANR) through the B2C project (contract ANR-19-CE01-0024-
573 01), by the French National program LEFE-CHAT (Les Enveloppes Fluides et l'Environnement – Chimie
574 Atmosphérique) through the BACON project. It has been also supported by DIM Qi² and Paris Ile-de-France Region. L.
575 Renzi and M. Zanatta were partially supported by ITINERIS project (IR0000032), the Italian Integrated Environmental
576 Research Infrastructures System (D.D. n. 130/2022 - CUP B53C22002150006) Funded by EU - Next Generation EU
577 PNRR- Mission 4 "Education and Research". The measurements at Monte Cimone were carried out within ACTRIS RI
578 and supported by the Italian Ministry project PER_ACTRIS_IT, under PNIR (Piano Nazionale Infrastrutture di Ricerca)
579 2014 – 2020.

580 11 References:

- 581 Anderson, T. L. and Ogren, J. A.: Determining Aerosol Radiative Properties Using the TSI 3563 Integrating
582 Nephelometer, *Aerosol Science and Technology*, 29, 57–69, <https://doi.org/10.1080/02786829808965551>, 1998.
- 583 Anderson, T. L., Covert, D. S., Marshall, S. F., Laucks, M. L., Charlson, R. J., Waggoner, A. P., Ogren, J. A., Caldow,
584 R., Holm, R. L., Quant, F. R., Sem, G. J., Wiedensohler, A., Ahlquist, N. A., and Bates, T. S.: Performance Characteristics
585 of a High-Sensitivity, Three-Wavelength, Total Scatter/Backscatter Nephelometer, *Journal of Atmospheric and Oceanic*
586 *Technology*, 13, 967–986, [https://doi.org/10.1175/1520-0426\(1996\)013<0967:PCOAHS>2.0.CO;2](https://doi.org/10.1175/1520-0426(1996)013<0967:PCOAHS>2.0.CO;2), 1996.
- 587 Andrews, E., Ogren, J. A., Bonasoni, P., Marinoni, A., Cuevas, E., Rodríguez, S., Sun, J. Y., Jaffe, D. A., Fischer, E. V.,
588 Baltensperger, U., Weingartner, E., Coen, M. C., Sharma, S., Macdonald, A. M., Leaitch, W. R., Lin, N.-H., Laj, P.,
589 Arsov, T., Kalapov, I., Jefferson, A., and Sheridan, P.: Climatology of aerosol radiative properties in the free troposphere,
590 *Atmospheric Research*, 102, 365–393, <https://doi.org/10.1016/j.atmosres.2011.08.017>, 2011.
- 591 Arnott, W. P., Hamasha, K., Moosmüller, H., Sheridan, P. J., and Ogren, J. A.: Towards aerosol light-absorption
592 measurements with a 7-wavelength aethalometer: Evaluation with a photoacoustic instrument and 3-wavelength
593 nephelometer, *Aerosol Science and Technology*, 39, 17–29, <https://doi.org/10.1080/027868290901972>, 2005.



- 594 Backman, J., Schmeisser, L., Virkkula, A., Ogren, J. A., Asmi, E., Starkweather, S., Sharma, S., Eleftheriadis, K., Uttal,
595 T., Jefferson, A., Bergin, M., Makshtas, A., Tunved, P., and Fiebig, M.: On Aethalometer measurement uncertainties and
596 an instrument correction factor for the Arctic, *Atmospheric Measurement Techniques*, 10, 5039–5062,
597 <https://doi.org/10.5194/amt-10-5039-2017>, 2017.
- 598 Baldo, C., Formenti, P., Di Biagio, C., Lu, G., Song, C., Cazaunau, M., Pangu, E., Doussin, J.-F., Dagsson-
599 Waldhauserova, P., Arnalds, O., Beddows, D., MacKenzie, A. R., and Shi, Z.: Complex refractive index and single
600 scattering albedo of Icelandic dust in the shortwave spectrum, *Aerosols/Laboratory Studies/Troposphere/Physics*
601 (physical properties and processes), <https://doi.org/10.5194/egusphere-2023-276>, 2023.
- 602 Bernardoni, V., Ferrero, L., Bolzacchini, E., Forello, A. C., Gregorič, A., Massabò, D., Močnik, G., Prati, P., Rigler, M.,
603 Santagostini, L., Soldan, F., Valentini, S., Valli, G., and Vecchi, R.: Determination of Aethalometer multiple-scattering
604 enhancement parameters and impact on source apportionment during the winter 2017/18 EMEP/ACTRIS/COLOSSAL
605 campaign in Milan, *Atmospheric Measurement Techniques*, 14, 2919–2940, <https://doi.org/10.5194/amt-14-2919-2021>,
606 2021.
- 607 Berry, G., Beckman, I., and Cho, H.: A comprehensive review of particle loading models of fibrous air filters, *Journal of*
608 *Aerosol Science*, 167, 106078, <https://doi.org/10.1016/j.jaerosci.2022.106078>, 2023.
- 609 Bescond, A., Yon, J., Ouf, F.-X., Rozé, C., Coppalle, A., Parent, P., Ferry, D., and Laffon, C.: Soot optical properties
610 determined by analyzing extinction spectra in the visible near-UV: Toward an optical speciation according to constituents
611 and structure, *Journal of Aerosol Science*, 101, 118–132, <https://doi.org/10.1016/j.jaerosci.2016.08.001>, 2016.
- 612 Bond, T. C., Doherty, S. J., Fahey, D. W., Forster, P. M., Berntsen, T., DeAngelo, B. J., Flanner, M. G., Ghan, S., Kärcher,
613 B., Koch, D., Kinne, S., Kondo, Y., Quinn, P. K., Sarofim, M. C., Schultz, M. G., Schulz, M., Venkataraman, C., Zhang,
614 H., Zhang, S., Bellouin, N., Guttikunda, S. K., Hopke, P. K., Jacobson, M. Z., Kaiser, J. W., Klimont, Z., Lohmann, U.,
615 Schwarz, J. P., Shindell, D., Storelvmo, T., Warren, S. G., and Zender, C. S.: Bounding the role of black carbon in the
616 climate system: A scientific assessment, *Journal of Geophysical Research: Atmospheres*, 118, 5380–5552,
617 <https://doi.org/10.1002/jgrd.50171>, 2013.
- 618 Brégonzio-Rozier, L., Giorio, C., Siekmann, F., Pangu, E., Morales, S. B., Temime-Roussel, B., Gratien, A., Michoud,
619 V., Cazaunau, M., DeWitt, H. L., Tapparo, A., Monod, A., and Doussin, J.-F.: Secondary organic aerosol formation from
620 isoprene photooxidation during cloud condensation–evaporation cycles, *Atmospheric Chemistry and Physics*, 16, 1747–
621 1760, <https://doi.org/10.5194/acp-16-1747-2016>, 2016.
- 622 Caponi, L., Formenti, P., Massabò, D., Di Biagio, C., Cazaunau, M., Pangu, E., Chevaillier, S., Landrot, G., Andreae,
623 M. O., Kandler, K., Piketh, S., Saeed, T., Seibert, D., Williams, E., Balkanski, Y., Prati, P., and Doussin, J.-F.: Spectral-
624 and size-resolved mass absorption efficiency of mineral dust aerosols in the shortwave spectrum: a simulation chamber
625 study, *Atmospheric Chemistry and Physics*, 17, 7175–7191, <https://doi.org/10.5194/acp-17-7175-2017>, 2017.
- 626 Chung, C. E., Ramanathan, V., and Decremier, D.: Observationally constrained estimates of carbonaceous aerosol
627 radiative forcing, *Proceedings of the National Academy of Sciences*, 109, 11624–11629,
628 <https://doi.org/10.1073/pnas.1203707109>, 2012.
- 629 Collaud Coen, M., Weingartner, E., Apituley, A., Ceburnis, D., Fierz-Schmidhauser, R., Flentje, H., Henzing, J. S.,
630 Jennings, S. G., Moerman, M., Petzold, A., Schmid, O., and Baltensperger, U.: Minimizing light absorption measurement
631 artifacts of the Aethalometer: evaluation of five correction algorithms, *Atmospheric Measurement Techniques*, 3, 457–
632 474, <https://doi.org/10.5194/amt-3-457-2010>, 2010.
- 633 Corbin, J. C., Pieber, S. M., Czech, H., Zanatta, M., Jakobi, G., Massabò, D., Orasche, J., El Haddad, I., Mensah, A. A.,
634 Stengel, B., Drinovec, L., Mocnik, G., Zimmermann, R., Prévôt, A. S. H., and Gysel, M.: Brown and Black Carbon
635 Emitted by a Marine Engine Operated on Heavy Fuel Oil and Distillate Fuels: Optical Properties, Size Distributions, and
636 Emission Factors, *Journal of Geophysical Research: Atmospheres*, 123, 6175–6195,
637 <https://doi.org/10.1029/2017JD027818>, 2018.
- 638 Cristofanelli, P., Marinoni, A., Arduini, J., Bonafè, U., Calzolari, F., Colombo, T., Decesari, S., Duchi, R., Facchini, M.
639 C., Fierli, F., Finessi, E., Maione, M., Chiari, M., Calzolari, G., Messina, P., Orlandi, E., Roccato, F., and Bonasoni, P.:
640 Significant variations of trace gas composition and aerosol properties at Mt. Cimone during air mass transport from North
641 Africa – contributions from wildfire emissions and mineral dust, *Atmospheric Chemistry and Physics*, 9, 4603–
642 4619, <https://doi.org/10.5194/acp-9-4603-2009>, 2009.



- 643 Cristofanelli, P., Brattich, E., Decesari, S., Landi, T. C., Maione, M., Putero, D., Tositti, L., and Bonasoni, P.: The “O.
644 Vittori” Observatory at Mt. Cimone: A “Lighthouse” for the Mediterranean Troposphere, in: High-Mountain Atmospheric
645 Research : The Italian Mt. Cimone WMO/GAW Global Station (2165 m a.s.l.), edited by: Cristofanelli, P., Brattich, E.,
646 Decesari, S., Landi, T. C., Maione, M., Putero, D., Tositti, L., and Bonasoni, P., Springer International Publishing, Cham,
647 1–14, https://doi.org/10.1007/978-3-319-61127-3_1, 2018.
- 648 Cristofanelli, P., Trisolino, P., Calzolari, F., Busetto, M., Calidonna, C. R., Amendola, S., Arduini, J., Fratticioli, C.,
649 Hundal, R. A., Maione, M., Marcucci, F., Marinoni, A., Montaguti, S., Renzi, L., Roccato, F., Bonasoni, P., and Putero,
650 D.: Influence of wildfire emissions to carbon dioxide (CO₂) observed at the Mt. Cimone station (Italy, 2165 m asl): A
651 multi-year investigation, *Atmospheric Environment*, 330, 120577, <https://doi.org/10.1016/j.atmosenv.2024.120577>,
652 2024.
- 653 Cuesta-Mosquera, A., Močnik, G., Drinovec, L., Müller, T., Pfeifer, S., Minguillón, M. C., Briel, B., Buckley, P.,
654 Dudoitis, V., Fernández-García, J., Fernández-Amado, M., Ferreira De Brito, J., Riffault, V., Flentje, H., Heffernan, E.,
655 Kalivitis, N., Kalogridis, A.-C., Keernik, H., Marmureanu, L., Luoma, K., Marinoni, A., Pikridas, M., Schauer, G.,
656 Serfozo, N., Servomaa, H., Titos, G., Yus-Díez, J., Ziola, N., and Wiedensohler, A.: Intercomparison and characterization
657 of 23 Aethalometers under laboratory and ambient air conditions: procedures and unit-to-unit variabilities, *Atmospheric*
658 *Measurement Techniques*, 14, 3195–3216, <https://doi.org/10.5194/amt-14-3195-2021>, 2021.
- 659 De Haan, D. O., Hawkins, L. N., Jansen, K., Welsh, H. G., Pednekar, R., de Loera, A., Jimenez, N. G., Tolbert, M. A.,
660 Cazaunau, M., Gratien, A., Bergé, A., Panguí, E., Formenti, P., and Doussin, J.-F.: Glyoxal’s impact on dry ammonium
661 salts: fast and reversible surface aerosol browning, *Atmospheric Chemistry and Physics*, 20, 9581–9590,
662 <https://doi.org/10.5194/acp-20-9581-2020>, 2020.
- 663 Denjean, C., Formenti, P., Picquet-Varrault, B., Camredon, M., Panguí, E., Zapf, P., Katrib, Y., Giorio, C., Tapparo, A.,
664 Temime-Roussel, B., Monod, A., Aumont, B., and Doussin, J. F.: Aging of secondary organic aerosol generated from the
665 ozonolysis of α -pinene: effects of ozone, light and temperature, *Atmospheric Chemistry and Physics*, 15, 883–897,
666 <https://doi.org/10.5194/acp-15-883-2015>, 2015.
- 667 Di Biagio, C., Formenti, P., Doppler, L., Gaimoz, C., Grand, N., Ancellet, G., Attié, J.-L., Bucci, S., Dubuisson, P., Fierli,
668 F., Mallet, M., and Ravetta, F.: Continental pollution in the Western Mediterranean basin: large variability of the aerosol
669 single scattering albedo and influence on the direct shortwave radiative effect, *Atmos. Chem. Phys.*, 16, 10591–10607,
670 <https://doi.org/10.5194/acp-16-10591-2016>, 2016.
- 671 Di Biagio, C., Formenti, P., Cazaunau, M., Panguí, E., Marchand, N., and Doussin, J.-F.: Aethalometer multiple scattering
672 correction C_{ref} for mineral dust aerosols, *Atmospheric Measurement Techniques*, 10, 2923–2939,
673 <https://doi.org/10.5194/amt-10-2923-2017>, 2017.
- 674 Di Biagio, C., Formenti, P., Balkanski, Y., Caponi, L., Cazaunau, M., Panguí, E., Journet, E., Nowak, S., Andreae, M.
675 O., Kandler, K., Saeed, T., Piketh, S., Seibert, D., Williams, E., and Doussin, J.-F.: Complex refractive indices and single-
676 scattering albedo of global dust aerosols in the shortwave spectrum and relationship to size and iron content, *Atmospheric*
677 *Chemistry and Physics*, 19, 15503–15531, <https://doi.org/10.5194/acp-19-15503-2019>, 2019.
- 678 Drinovec, L., Močnik, G., Zotter, P., Prévôt, A. S. H., Ruckstuhl, C., Coz, E., Rupakheti, M., Sciare, J., Müller, T.,
679 Wiedensohler, A., and Hansen, A. D. A.: The “dual-spot” Aethalometer: an improved measurement of aerosol black
680 carbon with real-time loading compensation, *Atmospheric Measurement Techniques*, 8, 1965–1979,
681 <https://doi.org/10.5194/amt-8-1965-2015>, 2015.
- 682 Drinovec, L., Jagodič, U., Pirker, L., Škarabot, M., Kurtjak, M., Vidović, K., Ferrero, L., Visser, B., Röhrbein, J.,
683 Weingartner, E., Kalbermatter, D. M., Vasilatou, K., Bühlmann, T., Pascale, C., Müller, T., Wiedensohler, A., and
684 Močnik, G.: A dual-wavelength photothermal aerosol absorption monitor: design, calibration and performance,
685 *Atmospheric Measurement Techniques*, 15, 3805–3825, <https://doi.org/10.5194/amt-15-3805-2022>, 2022.
- 686 Favez, O., Weber, S., Petit, J.-E., Alleman, L., Albinet, A., Riffault, V., Chazeau, B., Amodeo, T., Salameh, D., Zhang,
687 Y., Srivastava, D., Samaké, A., Aujay-Plouzeau, R., Papin, A., Bonnaire, N., Boullanger, C., Chatain, M., Chevrier, F.,
688 Detournay, A., Dominik-Sègue, M., Falhun, R., Garbin, C., Gherzi, V., Grignion, G., Levigoureux, G., Pontet, S.,
689 Rangognio, J., Zhang, S., Besombes, J.-L., Conil, S., Uzu, G., Savarino, J. E., Marchand, N., Gros, V., Marchand, C.,
690 Jaffrezo, J.-L., and Leoz-Garziandia, E.: Overview of the French Operational Network for In Situ Observation of PM
691 Chemical Composition and Sources in Urban Environments (CARA Program), *Atmosphere*, 12, 207,
692 <https://doi.org/10.3390/atmos12020207>, 2021.



- 693 Ferrero, L., Bernardoni, V., Santagostini, L., Cogliati, S., Soldan, F., Valentini, S., Massabò, D., Močnik, G., Gregorič,
694 A., Rigler, M., Prati, P., Bigogno, A., Losi, N., Valli, G., Vecchi, R., and Bolzacchini, E.: Consistent determination of the
695 heating rate of light-absorbing aerosol using wavelength- and time-dependent Aethalometer multiple-scattering
696 correction, *Science of the Total Environment*, 791, undefined-undefined,
697 <https://doi.org/10.1016/j.scitotenv.2021.148277>, 2021.
- 698 Fialho, P., Hansen, A. D. A., and Honrath, R. E.: Absorption coefficients by aerosols in remote areas: a new approach to
699 decouple dust and black carbon absorption coefficients using seven-wavelength Aethalometer data, *Journal of Aerosol*
700 *Science*, 36, 267–282, <https://doi.org/10.1016/j.jaerosci.2004.09.004>, 2005.
- 701 Formenti, P., Rajot, J. L., Desboeufs, K., Saïd, F., Grand, N., Chevaillier, S., and Schmechtig, C.: Airborne observations
702 of mineral dust over western Africa in the summer Monsoon season: spatial and vertical variability of physico-chemical
703 and optical properties, *Atmospheric Chemistry and Physics*, 11, 6387–6410, <https://doi.org/10.5194/acp-11-6387-2011>,
704 2011.
- 705 Freedman, D. and Diaconis, P.: On the histogram as a density estimator: L 2 theory, *Z. Wahrscheinlichkeitstheorie verw*
706 *Gebiete*, 57, 453–476, <https://doi.org/10.1007/BF01025868>, 1981.
- 707 Hansen, A. D. A., Rosen, H., and Novakov, T.: The aethalometer - An instrument for the real-time measurement of optical
708 absorption by aerosol particles, *Science of the Total Environment*, The, 36, 191–196, 1984.
- 709 Heuser, J., Di Biagio, C., Yon, J., Cazaunau, M., Bergé, A., Pangui, E., Zanatta, M., Renzi, L., Marinoni, A., Inomata, S.,
710 Yu, C., Bernardoni, V., Chevaillier, S., Ferry, D., Laj, P., Maillé, M., Massabò, D., Mazzei, F., Noyalet, G., Tanimoto,
711 H., Temime-Roussel, B., Vecchi, R., Vernocchi, V., Formenti, P., Picquet-Varrault, B., and Doussin, J.-F.: Spectral
712 optical properties of soot: laboratory investigation of propane flame particles and their link to composition,
713 <https://doi.org/10.5194/egusphere-2024-2381>, 9 October 2024.
- 714 Hinds, W. C.: *Aerosol Technology: Properties, Behavior, and Measurement of Airborne Particles*, John Wiley & Sons,
715 504 pp., 1999.
- 716 Huang, S.-H., Chen, C.-W., Kuo, Y.-M., Lai, C.-Y., McKay, R., and Chen, C.-C.: Factors Affecting Filter Penetration
717 and Quality Factor of Particulate Respirators, *Aerosol Air Qual. Res.*, 13, 162–171,
718 <https://doi.org/10.4209/aaqr.2012.07.0179>, 2013.
- 719 Kalbermatter, D. M., Močnik, G., Drinovec, L., Visser, B., Röhrbein, J., Oscity, M., Weingartner, E., Hyvärinen, A.-P.,
720 and Vasilatou, K.: Comparing black-carbon- and aerosol-absorption-measuring instruments – a new system using lab-
721 generated soot coated with controlled amounts of secondary organic matter, *Atmospheric Measurement Techniques*, 15,
722 561–572, <https://doi.org/10.5194/amt-15-561-2022>, 2022.
- 723 Kok, J. F., Storelvmo, T., Karydis, V. A., Adebisi, A. A., Mahowald, N. M., Evan, A. T., He, C., and Leung, D. M.:
724 Mineral dust aerosol impacts on global climate and climate change, *Nat Rev Earth Environ*, 4, 71–86,
725 <https://doi.org/10.1038/s43017-022-00379-5>, 2023.
- 726 Lack, D. A., Cappa, C. D., Cross, E. S., Massoli, P., Ahern, A. T., Davidovits, P., and Onasch, T. B.: Absorption
727 Enhancement of Coated Absorbing Aerosols: Validation of the Photo-Acoustic Technique for Measuring the
728 Enhancement, *Aerosol Science and Technology*, 43, 1006–1012, <https://doi.org/10.1080/02786820903117932>, 2009.
- 729 Laing, J. R., Jaffe, D. A., and Sedlacek, A. J.: Comparison of filter-based absorption measurements of biomass burning
730 aerosol and background aerosol at the mt. Bachelor observatory, *Aerosol and Air Quality Research*, 20, 663–678,
731 <https://doi.org/10.4209/aaqr.2019.06.0298>, 2020.
- 732 Laj, P., Bigi, A., Rose, C., Andrews, E., Lund Myhre, C., Collaud Coen, M., Lin, Y., Wiedensohler, A., Schulz, M.,
733 Ogren, J. A., Fiebig, M., Gliß, J., Mortier, A., Pandolfi, M., Petäjä, T., Kim, S.-W., Aas, W., Putaud, J.-P., Mayol-Bracero,
734 O., Keywood, M., Labrador, L., Aalto, P., Ahlberg, E., Alados Arboledas, L., Alastuey, A., Andrade, M., Artíñano, B.,
735 Ausmeel, S., Arsov, T., Asmi, E., Backman, J., Baltensperger, U., Bastian, S., Bath, O., Beukes, J. P., Brem, B. T.,
736 Bukowiecki, N., Conil, S., Couret, C., Day, D., Dayantolis, W., Degorska, A., Eleftheriadis, K., Fetzatzis, P., Favez, O.,
737 Flentje, H., Gini, M. I., Gregorič, A., Gysel-Beer, M., Hallar, A. G., Hand, J., Hoffer, A., Hueglin, C., Hooda, R. K.,
738 Hyvärinen, A., Kalapov, I., Kalivitis, N., Kasper-Giebl, A., Kim, J. E., Kouvarakis, G., Kranjc, I., Krejci, R., Kulmala,
739 M., Labuschagne, C., Lee, H.-J., Lihavainen, H., Lin, N.-H., Löschau, G., Luoma, K., Marinoni, A., Martins Dos Santos,
740 S., Meinhardt, F., Merkel, M., Metzger, J.-M., Mihalopoulos, N., Nguyen, N. A., Ondracek, J., Pérez, N., Perrone, M. R.,
741 Petit, J.-E., Picard, D., Pichon, J.-M., Pont, V., Prats, N., Prenni, A., Reisen, F., Romano, S., Sellegri, K., Sharma, S.,



- 742 Schauer, G., Sheridan, P., Sherman, J. P., Schütze, M., Schwerin, A., Sohmer, R., Sorribas, M., Steinbacher, M., Sun, J.,
743 Titos, G., et al.: A global analysis of climate-relevant aerosol properties retrieved from the network of Global Atmosphere
744 Watch (GAW) near-surface observatories, *Atmospheric Measurement Techniques*, 13, 4353–4392,
745 <https://doi.org/10.5194/amt-13-4353-2020>, 2020.
- 746 Li, J., Carlson, B. E., Yung, Y. L., Lv, D., Hansen, J., Penner, J. E., Liao, H., Ramaswamy, V., Kahn, R. A., Zhang, P.,
747 Dubovik, O., Ding, A., Lacis, A. A., Zhang, L., and Dong, Y.: Scattering and absorbing aerosols in the climate system,
748 *Nat Rev Earth Environ*, 3, 363–379, <https://doi.org/10.1038/s43017-022-00296-7>, 2022.
- 749 Liu, D., He, C., Schwarz, J. P., and Wang, X.: Lifecycle of light-absorbing carbonaceous aerosols in the atmosphere, *npj*
750 *Clim Atmos Sci*, 3, 1–18, <https://doi.org/10.1038/s41612-020-00145-8>, 2020a.
- 751 Liu, F., Yon, J., Fuentes, A., Lobo, P., Smallwood, G. J., and Corbin, J. C.: Review of recent literature on the light
752 absorption properties of black carbon: Refractive index, mass absorption cross section, and absorption function, *Aerosol*
753 *Science and Technology*, 54, 33–51, <https://doi.org/10.1080/02786826.2019.1676878>, 2020b.
- 754 Luoma, K., Virkkula, A., Aalto, P., Lehtipalo, K., Petäjä, T., and Kulmala, M.: Effects of different correction algorithms
755 on absorption coefficient – a comparison of three optical absorption photometers at a boreal forest site, *Atmospheric*
756 *Measurement Techniques*, 14, 6419–6441, <https://doi.org/10.5194/amt-14-6419-2021>, 2021.
- 757 Marinoni, A., Cristofanelli, P., Calzolari, F., Roccatò, F., Bonafè, U., and Bonasoni, P.: Continuous measurements of
758 aerosol physical parameters at the Mt. Cimone GAW Station (2165 m asl, Italy), *Science of The Total Environment*, 391,
759 241–251, <https://doi.org/10.1016/j.scitotenv.2007.10.004>, 2008.
- 760 Massabò, D., Bernardoni, V., Bove, M. C., Brunengo, A., Cuccia, E., Piazzalunga, A., Prati, P., Valli, G., and Vecchi, R.:
761 A multi-wavelength optical set-up for the characterization of carbonaceous particulate matter, *Journal of Aerosol Science*,
762 60, 34–46, <https://doi.org/10.1016/j.jaerosci.2013.02.006>, 2013.
- 763 Massabò, D., Caponi, L., Bernardoni, V., Bove, M. C., Brotto, P., Calzolari, G., Cassola, F., Chiari, M., Fedi, M. E.,
764 Fermo, P., Giannoni, M., Lucarelli, F., Nava, S., Piazzalunga, A., Valli, G., Vecchi, R., and Prati, P.: Multi-wavelength
765 optical determination of black and brown carbon in atmospheric aerosols, *Atmospheric Environment*, 108, 1–12,
766 <https://doi.org/10.1016/j.atmosenv.2015.02.058>, 2015.
- 767 Massoli, P., Murphy, D. M., Lack, D. A., Baynard, T., Brock, C. A., and Lovejoy, E. R.: Uncertainty in Light Scattering
768 Measurements by TSI Nephelometer: Results from Laboratory Studies and Implications for Ambient Measurements,
769 *Aerosol Science and Technology*, 43, 1064–1074, <https://doi.org/10.1080/02786820903156542>, 2009.
- 770 Massoli, P., Kebedian, P. L., Onasch, T. B., Hills, F. B., and Freedman, A.: Aerosol Light Extinction Measurements by
771 Cavity Attenuated Phase Shift (CAPS) Spectroscopy: Laboratory Validation and Field Deployment of a Compact Aerosol
772 Particle Extinction Monitor, *Aerosol Science and Technology*, 44, 428–435,
773 <https://doi.org/10.1080/02786821003716599>, 2010.
- 774 Modini, R. L., Corbin, J. C., Brem, B. T., Irwin, M., Bertò, M., Pileci, R. E., Fetfatizis, P., Eleftheriadis, K., Henzing, B.,
775 Moerman, M. M., Liu, F., Müller, T., and Gysel-Beer, M.: Detailed characterization of the CAPS single-scattering albedo
776 monitor (CAPS PMssa) as a field-deployable instrument for measuring aerosol light absorption with the extinction-minus-
777 scattering method, *Atmospheric Measurement Techniques*, 14, 819–851, <https://doi.org/10.5194/amt-14-819-2021>, 2021.
- 778 Moore, R. H., Ziemba, L. D., Dutcher, D., Beyersdorf, A. J., Chan, K., Crumeyrolle, S., Raymond, T. M., Thornhill, K.
779 L., Winstead, E. L., and Anderson, B. E.: Mapping the Operation of the Miniature Combustion Aerosol Standard (Mini-
780 CAST) Soot Generator, *Aerosol Science and Technology*, 48, 467–479, <https://doi.org/10.1080/02786826.2014.890694>,
781 2014.
- 782 Moschos, V., Gysel-Beer, M., Modini, R. L., Corbin, J. C., Massabò, D., Costa, C., Danelli, S. G., Vlachou, A.,
783 Daellenbach, K. R., Szidat, S., Prati, P., Prévôt, A. S. H., Baltensperger, U., and El Haddad, I.: Source-specific light
784 absorption by carbonaceous components in the complex aerosol matrix from yearly filter-based measurements, *Atmos.*
785 *Chem. Phys.*, 21, 12809–12833, <https://doi.org/10.5194/acp-21-12809-2021>, 2021.
- 786 Moteki, N.: Climate-relevant properties of black carbon aerosols revealed by in situ measurements: a review, *Prog Earth*
787 *Planet Sci*, 10, 12, <https://doi.org/10.1186/s40645-023-00544-4>, 2023.



- 788 Moteki, N., Kondo, Y., Nakayama, T., Kita, K., Sahu, L. K., Ishigai, T., Kinase, T., and Matsumi, Y.: Radiative transfer
789 modeling of filter-based measurements of light absorption by particles: Importance of particle size dependent penetration
790 depth, *Journal of Aerosol Science*, 41, 401–412, <https://doi.org/10.1016/j.jaerosci.2010.02.002>, 2010.
- 791 Nakayama, T., Kondo, Y., Moteki, N., Sahu, L. K., Kinase, T., Kita, K., and Matsumi, Y.: Size-dependent correction
792 factors for absorption measurements using filter-based photometers: PSAP and COSMOS, *Journal of Aerosol Science*,
793 41, 333–343, <https://doi.org/10.1016/j.jaerosci.2010.01.004>, 2010.
- 794 Ohata, S., Mori, T., Kondo, Y., Sharma, S., Hyvärinen, A., Andrews, E., Tunved, P., Asmi, E., Backman, J., Servomaa,
795 H., Veber, D., Eleftheriadis, K., Vratolis, S., Krejci, R., Zieger, P., Koike, M., Kanaya, Y., Yoshida, A., Moteki, N., Zhao,
796 Y., Tobo, Y., Matsushita, J., and Oshima, N.: Estimates of mass absorption cross sections of black carbon for filter-based
797 absorption photometers in the Arctic, *Atmospheric Measurement Techniques*, 14, 6723–6748,
798 <https://doi.org/10.5194/amt-14-6723-2021>, 2021.
- 799 Onasch, T. B., Massoli, P., Keabian, P. L., Hills, F. B., Bacon, F. W., and Freedman, A.: Single Scattering Albedo
800 Monitor for Airborne Particulates, *Aerosol Science and Technology*, 49, 267–279,
801 <https://doi.org/10.1080/02786826.2015.1022248>, 2015.
- 802 Petzold, A. and Schönlinner, M.: Multi-angle absorption photometry - A new method for the measurement of aerosol
803 light absorption and atmospheric black carbon, *Journal of Aerosol Science*, 35, 421–441,
804 <https://doi.org/10.1016/j.jaerosci.2003.09.005>, 2004.
- 805 Petzold, A., Ogren, J. A., Fiebig, M., Laj, P., Li, S.-M., Baltensperger, U., Holzer-Popp, T., Kinne, S., Pappalardo, G.,
806 Sugimoto, N., Wehrli, C., Wiedensohler, A., and Zhang, X.-Y.: Recommendations for reporting “black carbon”
807 measurements, *Atmospheric Chemistry and Physics*, 13, 8365–8379, <https://doi.org/10.5194/acp-13-8365-2013>, 2013.
- 808 Ramanathan, V. and Carmichael, G.: Global and regional climate changes due to black carbon, *Nature Geosci*, 1, 221–
809 227, <https://doi.org/10.1038/ngeo156>, 2008.
- 810 Rodriguez, A. A., Rafla, M. A., Welsh, H. G., Pennington, E. A., Casar, J. R., Hawkins, L. N., Jimenez, N. G., de Loera,
811 A., Stewart, D. R., Rojas, A., Tran, M.-K., Lin, P., Laskin, A., Formenti, P., Cazaunau, M., Pangui, E., Doussin, J.-F.,
812 and De Haan, D. O.: Kinetics, Products, and Brown Carbon Formation by Aqueous-Phase Reactions of Glycolaldehyde
813 with Atmospheric Amines and Ammonium Sulfate, *J Phys Chem A*, 126, 5375–5385,
814 <https://doi.org/10.1021/acs.jpca.2c02606>, 2022.
- 815 Rovira, J., Savadkoobi, M., Chen, G. I., Močnik, G., Aas, W., Alados-Arboledas, L., Artiñano, B., Aurela, M., Backman,
816 J., Banerji, S., Beddows, D., Brem, B., Chazeau, B., Coen, M. C., Colombi, C., Conil, S., Costabile, F., Coz, E., de Brito,
817 J. F., Eleftheriadis, K., Favez, O., Flentje, H., Freney, E., Gregorič, A., Gysel-Beer, M., Harrison, R., Hueglin, C.,
818 Hyvärinen, A., Ivančić, M., Kalogridis, A.-C., Keernik, H., Konstantinos, G., Laj, P., Liakakou, E., Lin, C., Listrani, S.,
819 Luoma, K., Maasikmets, M., Manninen, H. E., Marchand, N., dos Santos, S. M., Mbengue, S., Mihalopoulos, N., Nicolae,
820 D., Niemi, J. V., Norman, M., Ovadnevaite, J., Petit, J.-E., Platt, S., Prévôt, A. S. H., Pujadas, M., Putaud, J.-P., Riffault,
821 V., Rigler, M., Rinaldi, M., Schwarz, J., Silvergren, S., Teinmaa, E., Teinilä, K., Timonen, H., Titos, G., Tobler, A.,
822 Vasilescu, J., Vratolis, S., Yttri, K. E., Yubero, E., Zíková, N., Alastuey, A., Petäjä, T., Querol, X., Yus-Díez, J., and
823 Pandolfi, M.: A European aerosol phenomenology – 9: Light absorption properties of carbonaceous aerosol particles
824 across surface Europe, *Environment International*, 195, 109185, <https://doi.org/10.1016/j.envint.2024.109185>, 2025.
- 825 Samset, B. H., Stjern, C. W., Andrews, E., Kahn, R. A., Myhre, G., Schulz, M., and Schuster, G. L.: Aerosol Absorption:
826 Progress Towards Global and Regional Constraints, *Curr Clim Change Rep*, 4, 65–83, [https://doi.org/10.1007/s40641-](https://doi.org/10.1007/s40641-018-0091-4)
827 018-0091-4, 2018.
- 828 Sand, M., Samset, B. H., Myhre, G., Glib, J., Bauer, S. E., Bian, H., Chin, M., Checa-Garcia, R., Ginoux, P., Kipling, Z.,
829 Kirkevåg, A., Kokkola, H., Le Sager, P., Lund, M. T., Matsui, H., van Noije, T., Olivie, D. J. L., Remy, S., Schulz, M.,
830 Stier, P., Stjern, C. W., Takemura, T., Tsigaridis, K., Tsyro, S. G., and Watson-Parris, D.: Aerosol absorption in global
831 models from AeroCom phase III, *Atmospheric Chemistry and Physics*, 21, 15929–15947, [https://doi.org/10.5194/acp-21-](https://doi.org/10.5194/acp-21-15929-2021)
832 15929-2021, 2021.
- 833 Sandradewi, J., Prévôt, A. S. H., Szidat, S., Perron, N., Alfarra, M. R., Lanz, V. A., Weingartner, E., and Baltensperger,
834 U.: Using Aerosol Light Absorption Measurements for the Quantitative Determination of Wood Burning and Traffic
835 Emission Contributions to Particulate Matter, *Environ. Sci. Technol.*, 42, 3316–3323, <https://doi.org/10.1021/es702253m>,
836 2008.



- 837 Saturno, J., Pöhlker, C., Massabò, D., Brito, J., Carbone, S., Cheng, Y., Chi, X., Ditas, F., Hrabě de Angelis, I., Morán-
838 Zuloaga, D., Pöhlker, M. L., Rizzo, L. V., Walter, D., Wang, Q., Artaxo, P., Prati, P., and Andreae, M. O.: Comparison
839 of different Aethalometer correction schemes and a reference multi-wavelength absorption technique for ambient aerosol
840 data, *Atmospheric Measurement Techniques*, 10, 2837–2850, <https://doi.org/10.5194/amt-10-2837-2017>, 2017.
- 841 Savadkoobi, M., Pandolfi, M., Reche, C., Niemi, J. V., Mooibroek, D., Titos, G., Green, D. C., Tremper, A. H., Hueglin,
842 C., Liakakou, E., Mihalopoulos, N., Stavroulas, I., Artiñano, B., Coz, E., Alados-Arboledas, L., Beddows, D., Riffault,
843 V., De Brito, J. F., Bastian, S., Baudic, A., Colombi, C., Costabile, F., Chazeau, B., Marchand, N., Gómez-Amo, J. L.,
844 Estellés, V., Matos, V., van der Gaag, E., Gille, G., Luoma, K., Manninen, H. E., Norman, M., Silvergren, S., Petit, J.-E.,
845 Putaud, J.-P., Rattigan, O. V., Timonen, H., Tuch, T., Merkel, M., Weinhold, K., Vratolis, S., Vasilescu, J., Favez, O.,
846 Harrison, R. M., Laj, P., Wiedensohler, A., Hopke, P. K., Petäjä, T., Alastuey, A., and Querol, X.: The variability of mass
847 concentrations and source apportionment analysis of equivalent black carbon across urban Europe, *Environment*
848 *International*, 178, 108081, <https://doi.org/10.1016/j.envint.2023.108081>, 2023.
- 849 Schmid, O., Artaxo, P., Arnott, W. P., Chand, D., Gatti, L. V., Frank, G. P., Hoffer, A., Schnaiter, M., and Andreae, M.
850 O.: Spectral light absorption by ambient aerosols influenced by biomass burning in the Amazon Basin. I: Comparison
851 and field calibration of absorption measurement techniques, *Atmospheric Chemistry and Physics*, 6, 3443–3462,
852 <https://doi.org/10.5194/acp-6-3443-2006>, 2006.
- 853 Sturges, H. A.: The Choice of a Class Interval, *Journal of the American Statistical Association*, 21, 65–66,
854 <https://doi.org/10.1080/01621459.1926.10502161>, 1926.
- 855 Valentini, S., Barnaba, F., Bernardoni, V., Calzolari, G., Costabile, F., Di Liberto, L., Forello, A. C., Gobbi, G. P.,
856 Gualtieri, M., Lucarelli, F., Nava, S., Petralia, E., Valli, G., Wiedensohler, A., and Vecchi, R.: Classifying aerosol particles
857 through the combination of optical and physical-chemical properties: Results from a wintertime campaign in Rome (Italy),
858 *Atmospheric Research*, 235, 104799, <https://doi.org/10.1016/j.atmosres.2019.104799>, 2020.
- 859 Virkkula, A., Chi, X., Ding, A., Shen, Y., Nie, W., Qi, X., Zheng, L., Huang, X., Xie, Y., Wang, J., Petäjä, T., and
860 Kulmala, M.: On the interpretation of the loading correction of the aethalometer, *Atmospheric Measurement Techniques*,
861 8, 4415–4427, <https://doi.org/10.5194/amt-8-4415-2015>, 2015.
- 862 Vogel, F., Putero, D., Bonasoni, P., Cristofanelli, P., Zanatta, M., and Marinoni, A.: Saharan dust transport event
863 characterization in the Mediterranean atmosphere using 21 years of in-situ observations,
864 <https://doi.org/10.5194/egusphere-2025-1278>, 27 March 2025.
865
- 866 Wang, J., Doussin, J. F., Perrier, S., Perraudin, E., Katrib, Y., Pangu, E., and Picquet-Varrault, B.: Design of a new multi-
867 phase experimental simulation chamber for atmospheric photosmog, aerosol and cloud chemistry research, *Atmospheric*
868 *Measurement Techniques*, 4, 2465–2494, <https://doi.org/10.5194/amt-4-2465-2011>, 2011.
- 869 Weingartner, E., Saathoff, H., Schnaiter, M., Streit, N., Bitnar, B., and Baltensperger, U.: Absorption of light by soot
870 particles: determination of the absorption coefficient by means of aethalometers, *Journal of Aerosol Science*, 34, 1445–
871 1463, [https://doi.org/10.1016/S0021-8502\(03\)00359-8](https://doi.org/10.1016/S0021-8502(03)00359-8), 2003.
- 872 Wiedensohler, A., Birmili, W., Nowak, A., Sonntag, A., Weinhold, K., Merkel, M., Wehner, B., Tuch, T., Pfeifer, S.,
873 Fiebig, M., Fjårraa, A. M., Asmi, E., Sellegri, K., Depuy, R., Venzac, H., Villani, P., Laj, P., Aalto, P., Ogren, J. A.,
874 Swietlicki, E., Williams, P., Roldin, P., Quincey, P., Hügl, C., Fierz-Schmidhauser, R., Gysel, M., Weingartner, E.,
875 Riccobono, F., Santos, S., Gröning, C., Faloony, K., Beddows, D., Harrison, R., Monahan, C., Jennings, S. G., O’Dowd,
876 C. D., Marinoni, A., Horn, H.-G., Keck, L., Jiang, J., Scheckman, J., McMurry, P. H., Deng, Z., Zhao, C. S., Moerman,
877 M., Henzing, B., de Leeuw, G., Löschau, G., and Bastian, S.: Mobility particle size spectrometers: harmonization of
878 technical standards and data structure to facilitate high quality long-term observations of atmospheric particle number
879 size distributions, *Atmospheric Measurement Techniques*, 5, 657–685, <https://doi.org/10.5194/amt-5-657-2012>, 2012.
- 880 Yus-Díez, J., Bernardoni, V., Močnik, G., Alastuey, A., Ciniglia, D., Ivančić, M., Querol, X., Perez, N., Reche, C., Rigler,
881 M., Vecchi, R., Valentini, S., and Pandolfi, M.: Determination of the multiple-scattering correction factor and its cross-
882 sensitivity to scattering and wavelength dependence for different AE33 Aethalometer filter tapes: a multi-instrumental
883 approach, *Atmospheric Measurement Techniques*, 14, 6335–6355, <https://doi.org/10.5194/amt-14-6335-2021>, 2021.
- 884 Yus-Díez, J., Drinovec, L., Alados-Arboledas, L., Titos, G., Bazo, E., Casans, A., Patrón, D., Querol, X., Gonzalez-
885 Romero, A., Perez García-Pando, C., and Močnik, G.: Characterization of filter photometer artefacts in soot and dust
886 measurements & laboratory and ambient experiments using a traceably-calibrated aerosol absorption reference,
887 *EGUsphere*, 1–26, <https://doi.org/10.5194/egusphere-2024-3995>, 2025.



888 Zhu, C.-S., Qu, Y., Huang, H., Chen, J., Dai, W.-T., Huang, R.-J., and Cao, J.-J.: Black Carbon and Secondary Brown
889 Carbon, the Dominant Light Absorption and Direct Radiative Forcing Contributors of the Atmospheric Aerosols Over
890 the Tibetan Plateau, *Geophysical Research Letters*, 48, e2021GL092524, <https://doi.org/10.1029/2021GL092524>, 2021.

891